buildings

MDPI

Article

Application of Viscoelastic Dampers for Seismic Retrofitting of Existing Reinforced Concrete Buildings

Sennan Lee [1,2,*] and Chun Jiang [1,2]

[1] State Key Laboratory of Disaster Reduction in Civil Engineering, Tongji University, Shanghai 200092, China; jiangchun@tongji.edu.cn
[2] Department of Disaster Mitigation for Structures, Tongji University, Shanghai 200092, China
* Correspondence: sennanlee@gmail.com

Abstract

Passive control systems that provide both stiffness and energy dissipation, such as viscoelastic dampers (VEs), offer a promising strategy for seismic retrofit of existing reinforced concrete (RC) buildings, especially critical facilities that must remain operational during construction. Unlike conventional retrofit methods that require concrete casting and occupant evacuation, VE-based systems can be installed with shorter construction periods and reduced environmental disturbance. This study experimentally investigates the dynamic behavior of VE material subjected to large shear strain amplitudes of 300% and 400%, the latter exceeding typical design limits, to clarify its performance under severe seismic demands. The test results are used to calibrate a numerical model that represents the stiffness and energy-dissipation characteristics of the VE over this strain range. The calibrated model is then implemented in the seismic retrofit design of a six-story RC hospital building and evaluated through nonlinear structural analyses. The results indicate that the proposed VE retrofit scheme can achieve the targeted performance objectives and demonstrate the feasibility of applying high-strain VE dampers in practical seismic retrofit projects.

Keywords: seismic retrofit; viscoelastic damper; performance point; beyond design; numerical validation

1. Introduction

Many existing reinforced concrete (RC) buildings do not conform to current seismic design standards and thus require urgent retrofitting interventions [1,2]. The deficiencies in the moment and shear capacities of beams and columns are frequently attributed to concrete deterioration, inadequate reinforcement detailing, and the absence of modern seismic design considerations. An effective seismic retrofit strategy should aim to enhance the global seismic performance of the structural system, rather than merely reinforcing individual components [3]. Traditional retrofit approaches include the addition of RC shear walls [4], RC wing walls [5], or column jacketing [6], which have been widely used in practice. While the initial construction costs for these techniques may be relatively low, the secondary costs associated with interior and exterior finish restoration can be substantial, often discouraging building owners from pursuing these solutions. Furthermore, these methods must comply with numerous architectural and regulatory constraints [7,8]. For instance, new shear walls may obstruct emergency egress paths, new wing walls can reduce facade openings, and enlarged columns may necessitate the relocation of windows or doors. Even the use of steel bracing systems [9] may trigger similar concerns regarding architectural integrity and code compliance. Additionally, a key limitation of these

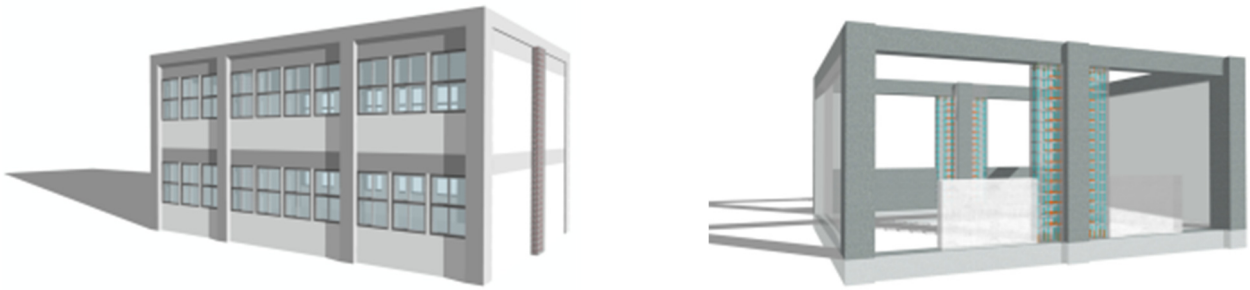
Check for updates

Academic Editor: Eric M. Lui

Received: 17 December 2025
Revised: 13 January 2026
Accepted: 20 January 2026
Published: 11 February 2026

Copyright: © 2026 by the authors. Licensee MDPI, Basel, Switzerland. This article is an open access article distributed under the terms and conditions of the Creative Commons Attribution (CC BY) license.

conventional techniques—commonly referred to as "wet construction methods"—is the need for occupant evacuation during concrete placement. This requirement renders such methods impractical for critical facilities that must remain operational year-round. Figure 1 summarizes the commonly adopted material-based seismic rehabilitation strategies for RC structures.



(**a**) (**b**)

Figure 1. Commonly adopted material-based seismic rehabilitation strategies for RC structures: (**a**) column jacketing; (**b**) adding wing walls.

The use of supplemental steel frames for seismic retrofitting of RC buildings has gained increasing attention in recent years [10]. This technique significantly reduces on-site construction time, as most of the fabrication and assembly processes are carried out in a controlled factory environment, thereby ensuring higher quality and consistency. The prefabricated steel components are subsequently transported to the construction site and installed using chemical anchorage systems. Strategically placing steel frames adjacent to the existing structural system allows for minimal interference with architectural features such as windows and emergency egress paths. Furthermore, this retrofit strategy generally presents fewer regulatory challenges and is more readily compliant with prevailing building codes [8]. Figure 2 illustrates typical steel frame-based seismic rehabilitation approaches.

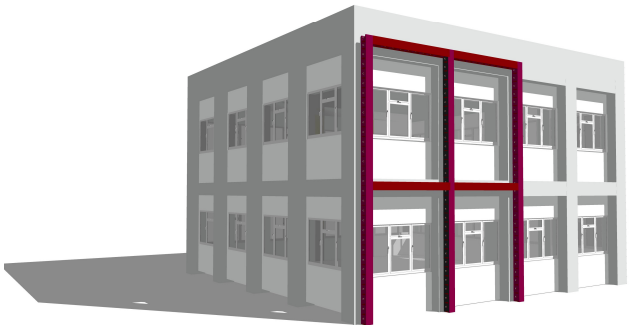


Figure 2. Typical steel frame-based seismic rehabilitation approach.

Aging RC buildings frequently exhibit insufficient reinforcement detailing. When supplemental steel elements are introduced for seismic retrofitting, they may induce excessive internal forces in the original structural members—such as beams, columns, beam–column joints, and foundations—during strong earthquakes. These induced forces may, in turn, accelerate damage or even trigger failure of existing RC components. In some cases, strengthening by adding steel beams and columns alone is insufficient to achieve satisfactory seismic performance. To mitigate this risk and to dissipate seismic energy more effectively, hysteretic energy dissipation devices can be integrated into the retrofit system; for example, steel panel dampers installed within an external steel framing system have been recommended as an effective solution [11]. While this approach can substantially

enhance the global seismic capacity and facilitate compliance with current seismic design codes, the long-term durability of the original RC members may still be a concern, because they can remain vulnerable to cumulative damage and accelerated deterioration under repeated strong shaking. Figure 3 illustrates the integration of steel panel dampers within external steel framing systems.



Figure 3. Additional steel panel dampers within external steel framing systems.

Beyond steel panel-type hysteretic dampers, a broad family of passive supplemental damping and energy-dissipation systems has been investigated and implemented for the seismic retrofit of existing RC buildings. These devices are commonly categorized as velocity-dependent dampers (e.g., fluid viscous dampers), displacement-dependent hysteretic devices (e.g., metallic yielding dampers such as slit dampers and shear panels), buckling-restrained braces (BRBs), friction dampers, and viscoelastic dampers (VEDs). Such retrofit strategies are attractive for operational facilities because they can provide substantial response reduction with limited "wet" strengthening work, while enabling performance-based objectives such as drift control, damage mitigation, and functional continuity [12–15].

Among these solutions, fluid viscous dampers (FVDs) have a mature application background and are supported by practical retrofit design methodologies and case study validations; recent studies further emphasize that their performance may be affected by thermo-mechanical coupling and system-level interaction details, which should be considered in analysis and design [16–19]. BRB-based retrofits represent another mainstream approach that provides stable hysteretic energy dissipation while simultaneously enhancing lateral strength and stiffness; research on RC frames has demonstrated their effectiveness, while also highlighting the importance of reliable force-transfer mechanisms and connection detailing for constructability and performance [20,21]. Compared with FVDs and BRBs, VEDs can offer combined stiffness and damping with potentially lower demand for major member strengthening, which makes them particularly relevant for retrofitting RC buildings that must remain in service. However, their rate- and temperature-dependent behavior necessitates careful experimental characterization and constitutive modeling to support credible seismic performance evaluation [12,15].

In this context, viscoelastic (VE) dampers provide an attractive alternative for seismic retrofitting because they can be installed using dry construction methods, introduce additional stiffness and energy dissipation, and be arranged with relatively minor interference to existing architectural layouts. While VE dampers have been widely applied in new buildings, their use in retrofitting aging RC structures—especially under large deformation demands—has been reported less frequently [22].

The present study investigates the application of Styrene-olefin-based VE dampers for the seismic retrofit of an existing six-story RC hospital building. First, laboratory tests

are conducted on small VE specimens to characterize their dynamic behavior under large shear strain amplitudes of 300% and 400%, including the effects of cyclic degradation and loading history. Second, an engineering-oriented data processing and calibration procedure is used to derive design values of equivalent stiffness and damping for specified strain and temperature conditions. Third, a seismic evaluation framework combining a remaining-life-based response spectrum and the capacity spectrum method is adopted for existing buildings. Finally, this framework is applied to the case-study hospital to design and assess a VE-based retrofit scheme, and the improved seismic performance of the retrofitted structure is demonstrated.

2. Materials and Methods

2.1. Viscoelastic Material and Test Program

The viscoelastic (VE) dampers adopted in this study employ a styrene–olefin-based high-damping elastomer. This copolymer-type thermoplastic elastomer exhibits both elastic and viscous behavior over the service temperature range relevant for building applications. Compared with conventional rubber-based materials, styrene–olefin-based elastomers provide larger allowable shear strains, reduced sensitivity of stiffness and damping to ambient temperature, and stable hysteretic behavior without pronounced strain hardening at large deformations [23–28]. These characteristics make them suitable for seismic energy dissipation devices that may be subjected to interstory drifts exceeding conventional design limits.

In the engineering interpretation, the rate-dependent shear response of the VE material is commonly idealized by an equivalent Kelvin–Voigt representation, i.e., a linear elastic spring in parallel with a viscous dashpot. In terms of shear stress $\tau(t)$ and shear strain $\gamma(t)$, the constitutive relation is written as

$$\tau(t) = G_{eq}\gamma(t) + \eta_{eq}\dot{\gamma}(t), \tag{1}$$

where G_{eq} is the effective shear modulus and η_{eq} is the effective viscosity. Under a constant shear stress τ_0, the shear strain evolves asymptotically to τ_0/G_{eq} as

$$\gamma(t) = \frac{\tau_0}{G_{eq}}\left[1 - \exp\left(-\frac{G_{eq}}{\eta_{eq}}t\right)\right], \quad \dot{\gamma}(0) = \frac{\tau_0}{\eta_{eq}}. \tag{2}$$

This retarded (delayed) elasticity leads, under cyclic shear loading, to a phase lag between $\tau(t)$ and $\gamma(t)$ and to an inclined elliptical hysteresis loop in the τ–γ plane, as schematically illustrated in Figures 4 and 5. The enclosed loop area quantifies the energy dissipated per cycle [23–28].

For structural analysis and design implementation, the damper is ultimately modeled using analysis-ready equivalent linear parameters (stiffness and damping) that are consistent with the experimentally observed behavior at the target shear strain level and temperature. In this study, these equivalent parameters are obtained by calibrating a generalized viscoelastic rheological representation and then reducing it to an equivalent Kelvin–Voigt form (K_{eq}, C_{eq}) at a representative circular frequency $\omega = 2\pi f$ for use in the building model. (The geometric conversion between material- and device-level parameters is $K_{eq} = (A/H)G_{eq}$ and $C_{eq} = (A/H)\eta_{eq}$, where A and H are the shear area and the VE layer thickness, respectively.) In common design software, each VED can be modeled as a linear spring (stiffness K_{eq}) acting in parallel with a linear viscous damper (coefficient C_{eq}) along the damper axis.

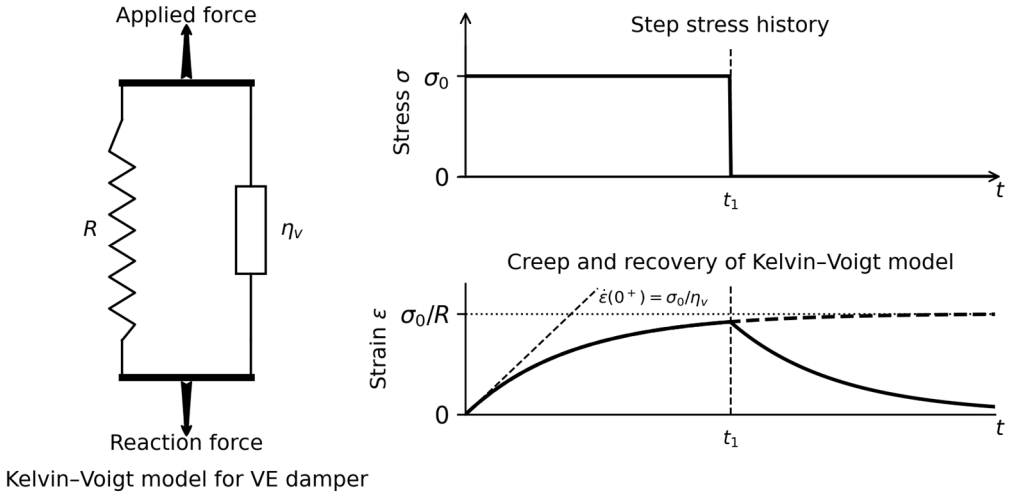


Figure 4. Kelvin model for VE dampers.

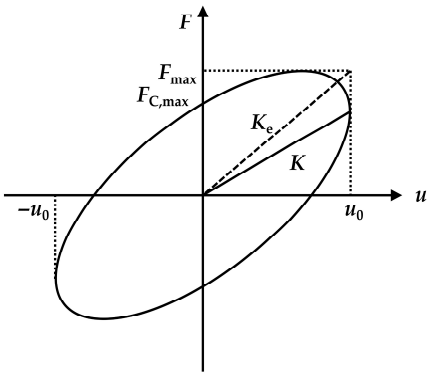


Figure 5. Hysteretic loop for typical VE dampers.

To characterize the mechanical properties of the adopted styrene–olefin-based VE material over a range of large shear strains, performance tests were conducted on small coupons using a servo-controlled universal testing machine. The objective was to clarify the effects of shear strain amplitude, temperature, and loading history on the equivalent stiffness and damping of the VE material at a representative excitation frequency. Each coupon specimen consisted of two VE layers, each with dimensions of 5 mm thickness, 70 mm length, and 40 mm width, bonded between steel plates to ensure uniform shear deformation. The total shear area A and thickness H of the VE material in the coupons correspond to a single "column" segment in the full-scale panel-type damper configuration.

The tests were performed in a temperature-controlled laboratory environment. Shear deformation was imposed by prescribing the relative displacement of the steel plates (displacement-controlled loading), and the corresponding shear force was measured by the load cell of the testing machine. The ambient temperature in the vicinity of the specimen and the actual operating temperature of the VE layers were monitored using thermocouples. Because the applied shear strain occasionally deviated slightly from the target values and the ambient temperature often differed from the nominal test temperature of 20 °C, the raw data were post-processed to compensate for temperature and shear-strain effects before being used to evaluate the mechanical parameters at the design temperature and design shear strain in accordance with established procedures [29–34].

For the cyclic loading program, the reference temperature was set at 20 °C and the loading period was fixed at 3 s, corresponding to a loading frequency of approximately 0.33 Hz. Sinusoidal loading histories were applied with the shear strain amplitude as

the control parameter, so as to capture the evolution of material properties under fixed displacement conditions at large deformation levels. Two shear strain amplitudes were considered, γ = 300% and γ = 400%. For each amplitude, two independent specimens were tested under two loading patterns: (1) continuous loading, in which the cycles were applied without interruption, and (2) interval loading, in which groups of 20 cycles were separated by rest periods of 24 h (denoted as "INT."). Notably, for a given amplitude, the continuous- and interval-loading specimens were subjected to an identical continuous loading history during the first 20 cycles; the two protocols diverged only after this common segment when the 24 h rest intervals were introduced in the INT. tests. From the measured force–displacement loops, the equivalent shear modulus G_{eff} and equivalent viscous damping ratio β_{eff} of the VE material were evaluated following standard definitions [29–34]. The resulting variations in G_{eff} and β_{eff} with loading cycles, deformation level, and loading pattern are presented in Section 3.

The loading period was fixed at 3 s ($f \approx 0.33$ Hz) to represent the dominant, low-frequency response expected when the case-study RC moment frame experiences large drift demands and stiffness degradation under strong earthquakes. In addition, adopting a relatively low excitation frequency helps reduce specimen self-heating and avoids overestimating rate-dependent properties during large-strain cycling. Accordingly, the present test program focuses on large-strain degradation and loading-history effects under a fixed representative frequency; the influence of excitation frequency is acknowledged as a limitation and warrants further investigation.

Finally, the test results at shear strain amplitudes of 300% and 400% were used to calibrate simple empirical expressions that relate the viscoelastic parameters to shear strain amplitude and temperature. Denoting by γ the shear strain amplitude, by A the total shear area of the VE material, by H its thickness, and by T the ambient temperature in degrees Celsius, the amplitude- and temperature-dependent stiffness and damping parameters of the VE model are represented by four coefficient functions,

$$k_1(T,\gamma), \quad c_1(T,\gamma), \quad c_2(T,\gamma), \quad k_0(T), \tag{3}$$

whose functional forms are summarized in Equations (4)–(7). These expressions adopt a normalized form proportional to A/H to account for geometric scaling and incorporate exponential temperature-dependence terms identified by least-squares regression of the test data. The specific numerical values of the regression coefficients are part of a proprietary design database provided by the manufacturer; therefore, only the functional forms and their calibration procedure are reported in this paper, while the coefficients themselves are not disclosed. Nonetheless, within the calibration range of γ = 300–400% and the relevant service temperature range, the fitted expressions reproduce the measured stiffness and damping trends with small regression errors and without systematic bias, providing a practical basis for engineering design calculations.

$$k_1(\gamma,T) = C_{k1}\frac{A}{H}\gamma^{\alpha_{k1}}\exp[\beta_{k1}(T-T_{\text{ref}})], \tag{4}$$

$$c_1(\gamma,T) = C_{c1}\frac{A}{H}\gamma^{\alpha_{c1}}\exp[\beta_{c1}(T-T_{\text{ref}})], \tag{5}$$

$$c_2(\gamma,T) = C_{c2}\frac{A}{H}\gamma^{\alpha_{c2}}\exp[\beta_{c2}(T-T_{\text{ref}})], \tag{6}$$

$$k_0(T) = C_{k0}\frac{A}{H}\exp[\beta_{k0}(T-T_{\text{ref}})], \tag{7}$$

where T_{ref} is a reference temperature (taken as 20 °C in this study), and $C_{(\cdot)}$, $\alpha_{(\cdot)}$, and $\beta_{(\cdot)}$ are regression coefficients identified from the test data. In Equations (4)–(7), the powers of γ and the exponential temperature-dependence coefficients are obtained from least-squares regression of the test results in logarithmic space. The normalization by A/H explicitly accounts for the geometric scaling of the viscoelastic layers. Using the least square fitting method, the key design parameters can be inferred accurately according to Equation (12).

Following the large-strain cyclic tests described above, analysis-ready damper parameters are required for the subsequent building-level modeling. In this study, the VE device is represented by a generalized rheological model consisting of (i) a Maxwell branch (spring K_1 in series with dashpot C_1), (ii) an additional dashpot C_2 in parallel, and (iii) a parallel bilinear spring K_2 to capture the stiffness transition at large shear strain. Section 2.2 describes the data processing and empirical calibration procedure used to evaluate these parameters as functions of shear strain amplitude and temperature, and to obtain the equivalent linear (K_{eq}, C_{eq}) used in the structural analyses at a representative frequency.

For a given shear-strain amplitude γ and temperature T, the parameters $K_1(\gamma,T)$, $C_1(\gamma,T)$, $C_2(\gamma,T)$, and $K_2(T)$ are evaluated from the calibrated empirical relations. At a representative circular frequency $\omega = 2\pi f$, the Maxwell branch is converted to an equivalent linear form with frequency-dependent stiffness and damping contributions:

$$K_M(\omega) = \frac{\omega^2 C_1^2 K_1}{K_1^2 + \omega^2 C_1^2}, \quad C_M(\omega) = \frac{K_1^2 C_1}{K_1^2 + \omega^2 C_1^2}. \tag{8}$$

The bilinear spring is represented by an amplitude-dependent secant stiffness $K_{2,\text{sec}}(\gamma)$ (equal to K_2 in the pre-yield range and reduced according to the post-yield stiffness ratio in the post-yield range). The resulting equivalent linear parameters used in the structural analysis are then

$$K_{eq}(\omega,\gamma,T) = K_M(\omega) + K_{2,\text{sec}}(\gamma), \quad C_{eq}(\omega,\gamma,T) = C_M(\omega) + C_2 + C_h(\gamma) \tag{9}$$

where $C_h(\gamma)$ denotes the equivalent viscous contribution associated with the hysteretic component of the bilinear spring (defined via energy equivalence). These K_{eq} and C_{eq} values are the quantities implemented in the building model.

2.2. Data Processing and Empirical Calibration of Viscoelastic Properties

2.2.1. Extraction of Equivalent Shear Modulus and Damping Ratio

The cyclic force–deformation loops obtained from the viscoelastic material tests were post-processed to extract the equivalent shear modulus G_{eff} and the equivalent damping ratio β_{eff} at each loading block. The equivalent shear modulus was defined as

$$G_{\text{eff}} = \frac{\Delta\tau}{\Delta\gamma}, \tag{10}$$

where $\Delta\tau$ and $\Delta\gamma$ are the peak-to-peak shear stress and shear strain in a given cycle, respectively. The equivalent damping ratio was evaluated from the hysteretic loop area E_{D} and the maximum elastic strain energy E_0 as

$$\beta_{\text{eff}} = \frac{1}{4\pi}\frac{E_D}{E_0}, \tag{11}$$

For each combination of target shear strain amplitude and temperature, the values of G_{eff} and β_{eff} obtained over repeated cycles were further normalized with respect to their initial-cycle values to facilitate comparison of degradation trends between different loading protocols. For engineering implementation, the design-effective properties were

selected using the 5-cycle/5% post-transient criterion defined in Section 3.1; for γ = 300%, the cycle-10 properties were adopted (or averaged over a narrow window around cycle 10).

2.2.2. Empirical Regression Model for Design Purposes

For engineering design, the dependence of the viscoelastic parameters on shear strain amplitude and temperature was represented by simple empirical relationships. Let P denote a generic viscoelastic parameter (e.g., storage shear modulus, loss modulus, or equivalent viscous coefficient) normalized by the geometric factor A/H, where A is the total shear area of the viscoelastic layers and H is their thickness. For each parameter P, the following strain–temperature-dependent functional form was adopted:

$$P(\gamma, T) = \frac{A}{H} C_P \gamma^{\alpha_P} \exp[\beta_P (T - T_{\text{ref}})], \tag{12}$$

where γ is the shear strain amplitude, T is the ambient temperature in degrees Celsius, T_{ref} = 20 °C is the reference temperature, and C_{P}, α_{P}, and β_{P} are regression coefficients calibrated from the test data for the specific Styrene-olefin-based material used in this study. Equation (12) was applied to four viscoelastic parameters, namely the storage and loss stiffness components and the equivalent viscous coefficients adopted in the Kelvin–Voigt representation of the damper.

2.2.3. Calibration Procedure and Goodness-of-Fit

The regression coefficients C_{P}, α_{P}, and β_{P} in Equation (12) were identified by least-squares fitting of the test data in logarithmic space. For each viscoelastic parameter P, all data points within the target engineering ranges,

$$2.0 \leq \gamma \leq 4.0, \text{ (corresponding to } 200\% - 400\% \text{ shear strain)} \quad 10\ ^\circ\text{C} \leq \text{T} \leq 30\ ^\circ\text{C}$$

were included in the calibration dataset. The quality of fit was evaluated by the normalized root-mean-square error (NRMSE),

$$\text{NRMSE}_P = \frac{\sqrt{\frac{1}{N}\sum_{i=1}^{N}(P_i^{\text{test}} - P_i^{\text{fit}})^2}}{\overline{P}^{\text{test}}}, \tag{13}$$

where P_i^{test} and P_i^{fit} denote the measured and fitted values, $\overline{P}^{\text{test}}$ is the mean of the measured values, and N is the number of data points. Over the calibration range, the NRMSE values were within approximately 5~8% for the stiffness-related parameters and 6~12% for the damping-related parameters, while the maximum absolute deviation at individual data points remained below about 20% of the measured value. These accuracy levels were deemed sufficient for engineering design of viscoelastic dampers in the present application.

The explicit numerical values of the regression coefficients are not listed in this paper because they form part of a proprietary material database jointly maintained by the manufacturer and the testing laboratory. Instead, the calibrated relationships are used to generate design values of the equivalent stiffness and damping for specified combinations of shear strain amplitude and temperature.

2.3. Design Method for VE Dampers and Connections

Viscoelastic dampers must be connected to the main structural members of the building, typically beams, regardless of whether they are installed in new construction or used as the primary components for seismic retrofit. In the retrofit scheme considered in this study, the VE dampers are mounted between the main beams of the upper and lower floors in the

vertical plane, with the damper body usually located at mid-story height. The damping force generated by each VE damper is applied at this mid-story elevation and is transmitted to the upper and lower beams, inducing additional forces and moments in the surrounding frame members, as schematically illustrated in Figure 6. In elevation, VE dampers are often arranged continuously along a bay; when dampers are connected to both the upper and lower sides of a beam, the resulting bending moment acting on the beam must account for the contributions from dampers above and below, such that the total additional moment can be expressed as $M_T = 2\,M_d$, where M_d is the moment generated by a single damper.

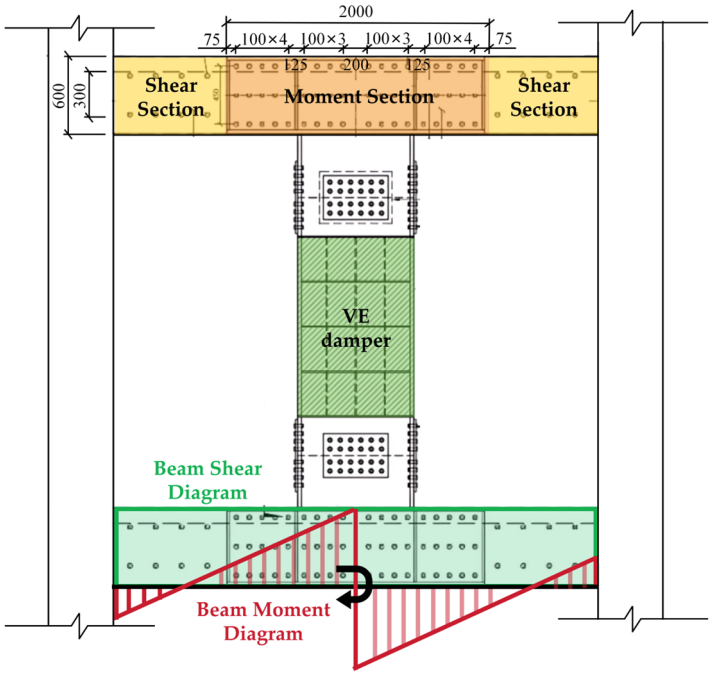


Figure 6. Shear force and moment in beams generated by VE dampers.

Embedded components are provided at the beam–damper interfaces to transfer the damping forces into the RC beams. These embedded components typically consist of vertical steel rods or rebars in combination with shear studs anchored into the concrete. The steel rods (or rebars) are designed to resist both the horizontal forces exerted by the damper and the associated bending moments. Because the horizontal force and bending moment act simultaneously, the steel rods (or rebars) are subjected to combined tension and shear; accordingly, their tensile strength should be reduced in design to account for the presence of shear stress. The shear studs, together with the steel rods (or rebars), jointly resist the horizontal damping force and ensure composite action between the steel connection plate and the RC beam.

The horizontal force from a damper is applied at a distance approximately equal to half the story height from the upper and lower structural beams, generating a bending moment that is transferred into the beams. The moment caused by the damping force can be evaluated as

$$M_d = F_d \times H_s/2 \tag{14}$$

where H_s is typically taken as half the story height or the actual vertical distance between the line of action of the damper force and the centroid of the beam, and F_d is the damping force generated by the VE damper. The diagrams in Figure 6 depict the distributions of bending moment and shear force in a beam segment flanked by columns when subjected to the equivalent concentrated moment M_T (shown as an arrow on the beam). The moment induced by the damping forces behaves similarly to a concentrated moment applied at

mid-span, resulting in an approximately triangular bending-moment distribution along the beam, whereas the corresponding shear force exhibits a nearly rectangular distribution. The peak bending moment within the beam is approximately $M_T/2$, and the associated shear force is about M_T/L, where L is the beam span. When checking the beam, the combined effects of dead load, live load, and the moment induced by the dampers should be considered.

Because the damping force generated by VE dampers is out of phase with the structural displacement response during seismic excitation, it is not necessary to combine the full seismic inertia forces and the peak damping forces simultaneously in a single load case. Instead, design verification is performed under three representative scenarios that correspond to different stages of the structural seismic response: maximum velocity, maximum displacement, and maximum acceleration.

Under the maximum velocity scenario, the structure is still within or close to the elastic range, and the deformation demand remains moderate while the interstory velocity reaches its peak. The peak damping force in this stage can be estimated as

$$F_D \approx C_{\text{eff}} 2\pi f_1 D, \tag{15}$$

where C_{eff} is the effective damping coefficient of the VE dampers, f_1 is the fundamental frequency of the structure, and D denotes the maximum interstory drift demand at the damper installation level, which was extracted from the nonlinear static pushover results at the CSM performance point (i.e., from the pushover step corresponding to the target displacement). D is used as an upper-bound deformation demand for conservative design checks of the supporting beams and embedded connections. The actual damper deformation u_d is obtained in the structural model directly as the relative displacement between the damper end nodes. Because beam-end rotation and connection flexibility may reduce the deformation transmitted to the VE layers, u_d is generally smaller than Δ_{story}. Therefore, using $D = \Delta_{\text{story}}$ intentionally overestimates the peak damper force for connection design, which is desirable because loss of the supporting members would lead to damper malfunction and compromise the retrofit performance. In this scenario, the load combination used for checking the beams, embedded components, and connections consists of dead load, live load, and the effects of the damping forces, without additional inelastic seismic demands.

Under the maximum displacement scenario, the structural displacements approach their peak values, but the interstory velocity is zero. At this instant, the VE dampers do not generate additional viscous forces, and the internal forces in the main structural members are governed by the inertial effects of the seismic action alone. Therefore, the design load combination for this scenario is essentially the same as that adopted in the original structural design, and the verification focuses on the capacity of the existing RC members to sustain the maximum displacement demand.

For the maximum acceleration scenario, lateral forces acting on the structure are influenced by both the displacement and velocity components of the response. In this study, the design force for the maximum acceleration case is defined as the superposition of the forces from the maximum displacement and maximum velocity cases, scaled by two factors CF_1 and CF_2 that depend on the equivalent viscous damping ratio β_{eff} of the VE dampers:

$$CF_1 = \cos[\tan - 1(2\beta_{\text{eff}})], \tag{16}$$

$$CF_2 = \sin[\tan - 1(2\beta_{\text{eff}})]. \tag{17}$$

Here, β_{eff} denotes the equivalent viscous damping ratio of the VE dampers, evaluated from their complex stiffness at the dominant vibration frequency, as defined in Section 2.2.

The factors CF_1 and CF_2 are used to weight the contributions from the displacement-controlled and velocity-controlled responses when constructing the design forces for the maximum acceleration condition. In this manner, the bending moments and shear forces in the main beams and damper connections can be consistently verified for different seismic demand levels, taking into account the additional damping provided by the VE devices.

If the main beam is relatively small, exhibits limited flexural stiffness, or if the VE damper is comparatively stiff, significant rotation may occur at the beam–damper interface. Such rotation can reduce the effective deformation imposed on the damper, because part of the interstory drift is absorbed by beam rotation instead of being transmitted as shear deformation to the VE material. When this effect is pronounced, the energy-dissipation efficiency of the damper is compromised. In these cases, the installation of diagonal braces at the damper connections can be considered. The braces increase the rotational stiffness at the connection, enhance the efficiency of transmitting interstory drift to the damper, and share a portion of the damping force, thereby improving both the structural response and the durability of the connection details. For high-rise buildings located in seismic-prone regions, where main beams and slabs are typically deep and stiff, diagonal braces are less frequently required. However, for smaller beams in low- to mid-rise buildings, bracing systems may be advantageous to ensure adequate rotational restraint and reliable force transfer at the VE damper connections.

The above procedure—comprising the evaluation of additional beam actions induced by VE dampers, the design of embedded components and shear studs, and the verification of beam and connection capacities under the three representative response scenarios—provides a consistent framework for designing VE damper connections in both new and existing RC buildings. This design method is subsequently applied to the case-study hospital building described in Section 2.5, and the corresponding retrofit performance is evaluated in Section 3.

2.4. Seismic Evaluation Framework for Existing RC Buildings

The seismic evaluation and retrofit design of the case-study hospital building follow an existing framework originally developed for reinforced concrete school buildings and later extended to other types of RC structures [35–37]. The framework combines (1) a remaining-life-based design spectrum derived from the new-building code spectrum, (2) a three-stage evaluation procedure ranging from preliminary screening to detailed analysis, and (3) a capacity spectrum method (CSM) formulated on the acceleration–displacement response spectrum (ADRS) plane [38,39]. This section summarizes the main features of the framework as applied in the present study.

2.4.1. Remaining-Life-Based Design Spectrum

For existing buildings, the seismic demand used for retrofit design is evaluated by scaling down the original code design spectrum according to the residual service life of the structure [35–37]. Instead of directly using the design parameters associated with a 475-year return period earthquake—such as the effective peak ground acceleration (EPA) and the 5% damped spectral acceleration parameters S_{DS} and S_{D1}—a reduced response spectrum is constructed for the expected remaining lifetime T of the building.

Let T_r denote the return period of the original design earthquake (e.g., 475 years) and let $a_{g,475}$ be the corresponding EPA on rock outcrop specified by the code [38]. The guidelines introduce a lifetime reduction factor $k_T = k(T/T_r)$, specified in tabular or functional form, which reflects the lower probability of exceedance during the shorter remaining life. The reduced EPA for the existing building is then obtained as

$$a_{g,r} = k_T a_{g,475}, \tag{18}$$

And the entire design spectrum is scaled accordingly, yielding reduced values of $S_{DS,r}$ and $S_{D1,r}$. The resulting "remaining-life-based spectrum" is used as the seismic demand for evaluating the as-built and retrofitted structures. In this way, the retrofit demand remains consistent with the probabilistic basis of the original code spectrum while explicitly accounting for the remaining service life of the building.

2.4.2. Three-Stage Evaluation Procedure

The overall evaluation and rehabilitation process is implemented in three stages, which differ in the level of detail, required expertise, and analytical effort [35–37].

- **Stage I: Preliminary Investigation.**

Stage I is carried out by the building owner or facility manager. Basic information such as construction year, structural system, number of stories, plan and elevation configuration, obvious irregularities, and visible deterioration (cracks, spalling, corrosion) is collected using standardized checklists. The aim is to identify buildings that clearly require no further action and those that may be potentially vulnerable and should proceed to Stage II.

- **Stage II: Initial Seismic Evaluation.**

Stage II is performed by engineers with a civil/structural background. Simplified evaluation methods—such as equivalent static analysis, index-type scoring procedures, or codified demand–capacity checks—are applied to estimate the lateral strength and deformation capacity of the building under the reduced design spectrum. If the seismic performance indices or strength checks satisfy prescribed threshold values, the building is judged adequate for the target performance level. Otherwise, a more detailed evaluation in Stage III is required.

- **Stage III: Detailed Seismic Evaluation.**

Stage III involves detailed material testing, refined structural modeling, and, when necessary, nonlinear analysis. In this stage, nonlinear static pushover analyses are performed, and the capacity curves are converted to capacity spectra on the ADRS plane. The seismic performance is then evaluated using the CSM, in which the capacity spectrum of the building is compared with the remaining-life-based demand spectrum derived in Section 2.4.1. This detailed evaluation determines whether the building satisfies the target performance objectives or requires seismic rehabilitation.

In the present study, the hospital building has already been identified as requiring Stage III evaluation based on Stage I–II screening and in situ material tests (Section 3.2). Therefore, the following subsection focuses on the CSM adopted in Stage III.

2.4.3. Capacity Spectrum Method on the ADRS Plane

The detailed performance evaluation in Stage III follows a capacity spectrum method similar to the procedures recommended in ATC-40 and related guidelines [37–39]. The method consists of three main steps: (i) transformation of the multi-degree-of-freedom (MDOF) pushover capacity curve into an equivalent single-degree-of-freedom (SDOF) capacity spectrum, (ii) determination of the performance point and the associated equivalent damping ratio, and (iii) comparison of the capacity and demand at the performance point.

(a) Transformation to capacity spectrum

A nonlinear static pushover analysis is first carried out to obtain the global capacity curve, i.e., the relationship between the base shear V_b and the roof displacement Δ_r. Let w_i and ϕ_{1i} denote the seismic weight and the first-mode lateral displacement at the i-th story,

and let $W = \Sigma_i w_i$ be the total seismic weight of the building. The first-mode participation factor PF_1 and the normalized first-mode amplitude at the roof α_1 are defined as

$$PF_1 = \frac{\sum_i w_i \phi_{1i}}{\sum_i w_i \phi_{1i}^2}, \quad \alpha_1 = \frac{\sum_i w_i \phi_{1i}}{W PF_1}. \tag{19}$$

With the first-mode shape normalized to unity at the roof, the capacity curve (V_b, Δ_r) is transformed into the ADRS plane by

$$S_a = \frac{V_b}{\alpha_1 W}, \quad S_d = \frac{\Delta_r}{PF_1}, \tag{20}$$

where S_a and S_d are the SDOF spectral acceleration and spectral displacement, respectively. The resulting curve in the (S_d, S_a) plane is referred to as the capacity spectrum.

(b) Performance point and equivalent damping

The capacity spectrum is plotted together with the remaining-life-based elastic demand spectrum corresponding to 5% viscous damping. The capacity spectrum is then idealized by a bilinear curve representing the elastic and inelastic portions of the response. The performance point ($S_{d,p}$, $S_{a,p}$) is defined as the intersection between the capacity spectrum and a damping-modified demand spectrum.

At a trial performance point, the equivalent period T_{eq} of the SDOF system is obtained from

$$T_{eq} = 2\pi \sqrt{\frac{S_{d,p}}{S_{a,p} g}} \tag{21}$$

where g is the gravitational acceleration. The total equivalent damping ratio ξ_{eq} at the performance point is decomposed into three contributions [37–39]:

(i) Baseline viscous damping of the bare structure, typically taken as $\xi_0 = 0.05$;

(ii) Hysteretic damping ξ_h arising from inelastic behavior of the structural members, evaluated from the area of the equivalent SDOF hysteresis loop;

(iii) Additional viscous damping ξ_{VE} provided by the VE dampers.

The contribution of the VE dampers to the first-mode damping ratio is evaluated as

$$\xi_{VE} = \frac{T \sum_j C_j \phi_{rj}^2 \cos^2 \theta_j}{4\pi \sum_i m_i \phi_i^2}, \tag{22}$$

where T is the fundamental period of the damped structure; C_j is the equivalent viscous damping coefficient of the VE damper(s) at story j; θ_j is the installation angle of the VE damper; ϕ_{rj} is the first-mode relative horizontal displacement between the two ends of the damper at story j; m_i is the lumped mass at story iii; and ϕ_{1j} is the first-mode lateral displacement at story i. The numerator represents the first-mode modal damping coefficient associated with the VE dampers, and the denominator represents the corresponding first-mode modal mass.

The total equivalent damping ratio is then obtained as

$$\xi_{eq} = \xi_0 + \kappa(\xi_h + \xi_{VE}) \tag{23}$$

where κ is a damping modification coefficient (typically $\kappa \approx 0.33$) accounting for the non-ideal shape of the hysteresis loops [39]. For a given trial value of ξ_{eq}, a damping-modified demand spectrum is constructed from the 5% damped remaining-life spectrum by applying code-specified damping modification factors $B_S(\xi_{eq})$ and $B_1(\xi_{eq})$ to the short- and long-

period branches, respectively [38]. The demand spectral acceleration corresponding to T_{eq} and ξ_{eq} is then read from this modified spectrum, and the performance point is updated accordingly. The procedure is iterated until convergence of ξ_{eq} and ($S_{d,p}$, $S_{a,p}$) is achieved. Note that ξ_{h} denotes the raw hysteretic damping ratio evaluated from the area of the equivalent SDOF hysteresis loop, whereas the term $\kappa\xi_{\mathrm{h}}$ in Equation (23) represents its effective contribution to ξ_{eq} after accounting for the non-ideal loop shape ($\kappa \approx 0.33$). For clarity, damping ratios are dimensionless and are reported in both decimal and percentage forms where appropriate.

Once the performance point ($S_{d,p}$, $S_{a,p}$) and ξ_{eq} converge, the effective peak ground acceleration index A_p associated with the performance point is obtained by inverting the damping-modified design spectrum specified in the current building code [38]. For the spectrum shape adopted in [38], A_p can be computed as

$$A_p = \begin{cases} \dfrac{S_{a,p}}{1+\left(\frac{2.5}{B_S}-1\right)\frac{T_{eq}}{0.2T_0}}, & T_{eq} \le 0.2T_0 \\ \dfrac{B_S}{2.5}S_{a,p}, & 0.2T_0 < T_{eq} \le T_0 \\ \dfrac{B_S T_{eq}}{2.5T_0}S_{a,p}, & T_{eq} > T_0 \end{cases} \quad (24)$$

where $S_{a,p}$ is the spectral acceleration at the performance point; T_{eq} is the equivalent period defined in Equation (19); T_0 is the transition period of the damping-modified spectrum, calculated as $T_0 = SD_1B_S/(SD_SB_1)$; SD_S and SD_1 are the 5%-damped spectral response acceleration parameters at short periods and at $T = 1$ s, respectively; and B_S and B_1 are the damping modification factors tabulated as functions of ξ_{eq} in the building code [38], obtained by interpolation.

(c) Performance check and need for retrofit

Once the converged performance point is obtained, the seismic capacity of the building is evaluated by comparing the spectral acceleration at the performance point with the remaining-life-based demand spectrum. If the peak ground acceleration index associated with the performance point exceeds or equals the reduced EPA, the building is judged to satisfy the target performance level; otherwise, seismic rehabilitation measures such as the installation of VE dampers are required [35–37]. In the present study, this CSM-based procedure is applied to both the original and retrofitted configurations of the hospital building to quantify the improvement in seismic performance achieved by the VE retrofit scheme.

2.5. Case-Study Building and Numerical Modeling

A six-story reinforced concrete (RC) hospital building is adopted as the case study, and its architectural layout is shown in Figure 7. The building is a moment-resisting frame (MRF) has been in service for more than 40 years and functions as a local medical facility in New Taipei City, Taiwan. The concrete compressive strength is $f_{\mathrm{c}}{}' = 20.7$ MPa (3000 psi), and the reinforcing steel is Grade 60 with $f_{\mathrm{y}} = 420$ MPa (60 ksi). The frame columns are 60 × 60 cm, the typical primary beams participating in lateral resistance are 400 × 700 mm, and the floor slabs are 20 cm thick. The original structural design followed the seismic code provisions then in force, which correspond to a 5%-damped short-period spectral acceleration parameter $S_{\mathrm{DS}} = 0.60$, an effective peak ground acceleration (EPA) of 0.24 g, and a transition period $T_0 = 1.62$ s for a 475-year return period earthquake [38]. For the purpose of seismic evaluation of this existing building, the remaining-life-based design spectrum introduced in Section 2.4.1 is adopted. Assuming an expected residual service life of 20 years, the EPA is rationally reduced using the formulas in Section 2.4.1, yielding a reduced EPA value a_{gr} and the corresponding adjusted spectral acceleration parameters. Figure 8 compares the original response spectrum for newly designed buildings

with the reduced spectrum used for the seismic assessment and retrofit design of the case-study hospital.

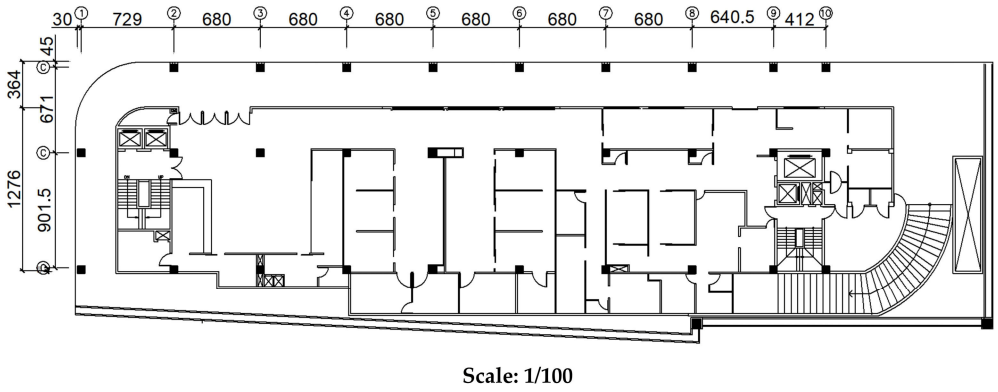


Figure 7. Architectural design of the hospital building example. The span, for example, is 680 cm.

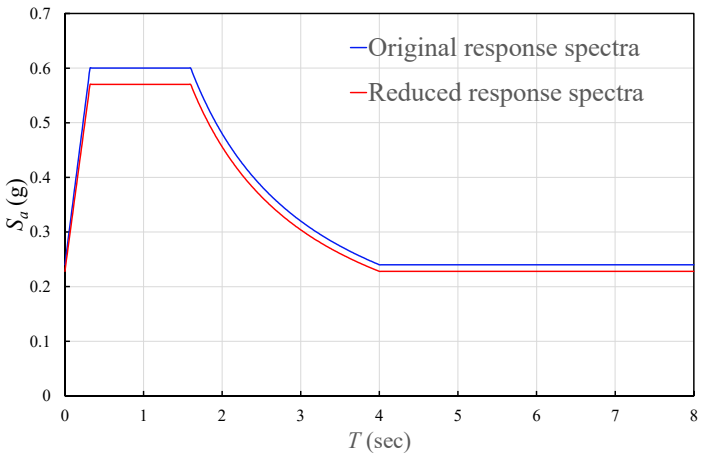


Figure 8. Original and reduced response spectra for new design and seismic retrofitting, respectively.

In addition to the CSM-based performance check, a practical deformation-related objective was adopted for engineering interpretation. Specifically, a target maximum interstory drift ratio of 1.5% at the CSM performance point was used as a supplementary indicator. Pushover analyses were conducted along both principal plan directions. For the as-built building, the maximum interstory drift ratio at the performance-point displacement was 0.52% in the X direction and 1.67% in the Y direction, indicating that the Y direction governs and exceeds the adopted drift target. Therefore, the retrofit design is driven by the Y-direction response, and only the Y-direction story drift profiles are presented in the Results section for brevity, while the key peak values in both directions are reported. Story drift ratios were extracted from the ETABS pushover results at the roof displacement corresponding to the converged CSM performance point.

To assess the existing condition of the RC members, in situ material tests were carried out on concrete cores extracted from each story. The measured compressive strengths and carbonation depths are summarized in Section 3.2 (see Figure 9) and are used to judge the current damage state and durability of the structural components, as well as to determine the necessity and urgency of seismic rehabilitation. These test results provide the basic material input parameters for the numerical model of the existing structure.

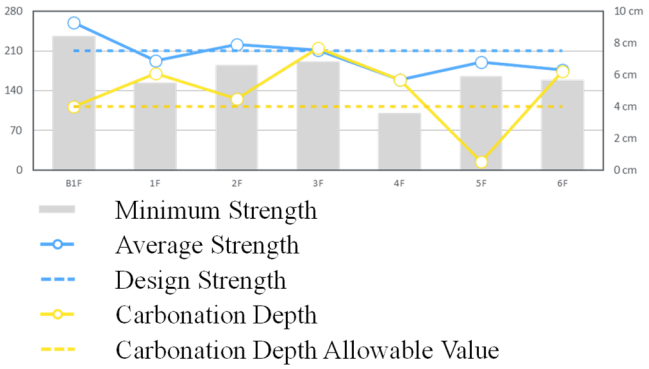


Figure 9. Current concrete strengths and carbonation depths of the hospital building example.

Given the critical function of the facility and the requirement to maintain hospital operations during construction, invasive strengthening techniques involving extensive demolition and casting of new concrete were considered impractical. To satisfy these practical constraints and to enhance both stiffness and energy dissipation, viscoelastic (VE) dampers are adopted as the primary retrofit measure. In addition to the VE dampers with a nominal maximum force capacity of 500 kN experimentally investigated in Section 3, dampers with capacities of 750 kN and 1000 kN are also used so that the retrofitted building can meet the current code requirements while allowing a feasible installation scheme. The final damper layout is illustrated in Figure 10, where VE panels are distributed along designated frames from the second to the fifth stories. Owing to their panel-type configuration, this arrangement is intended to transfer a large portion of the interstory drift to the VE layers, thereby improving deformation-transfer efficiency compared with brace-type layouts. In the numerical model, however, the actual damper deformation is obtained directly from the relative displacement of the damper end nodes and is not assumed to be identical to the story drift. At the same time, the damper forces introduce additional bending and shear demands on the supporting beams; therefore, these beams and their connections are checked in accordance with the design procedures in Section 2.2, and strengthened using steel plate jacketing wherever their flexural or shear capacities are found to be insufficient when the combined effects of damper-induced forces, self-weight, and live loads are considered.

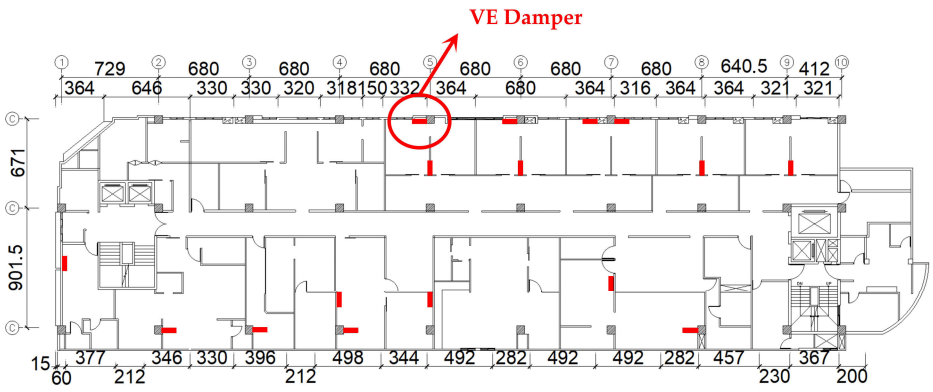


Figure 10. Construction routes and installation locations of VE dampers in the hospital building example. The span, for example, is 680 cm.

The seismic response of the hospital building, in both its original and retrofitted configurations, is analyzed using a three-dimensional numerical model developed in ETABS. Figure 11 presents the ETABS model of the hospital structure equipped with VE dampers. The existing RC members are modeled using frame and slab elements following standard building engineering practice, while mass is lumped at floor levels based on

tributary gravity loads. The VE dampers are modeled as Kelvin–Voigt-type elements that connect pairs of floor nodes in the damper bays, consistent with the rheological representation introduced in Section 2.1. In this formulation, each VE damper contributes both storage stiffness and viscous damping; consequently, the elastic stiffness of the damped (retrofitted) structure is slightly higher than that of the undamped (original) structure.

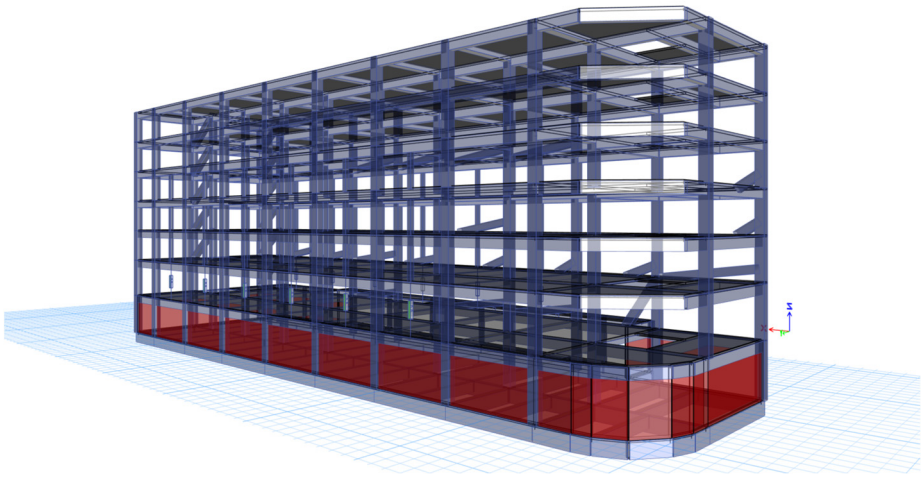


Figure 11. Structural model of the hospital building equipped with VE dampers.

An elastic eigenvalue modal analysis was conducted for both the as-built and retrofitted ETABS models. Table 1 reports the modal periods and the (cumulative) effective modal mass participation ratios in the two principal horizontal directions, and identifies the dominant translational modes used to define the modal lateral load patterns in the subsequent pushover analyses.

Table 1. Modal periods and effective mass.

Mode	As-Built			Retrofitted		
	Period (s)	Cumulative Effective Mass Ratio in X	Cumulative Effective Mass Ratio in Y	Period (s)	Cumulative Effective Mass Ratio in X	Cumulative Effective Mass Ratio in Y
1	1.67	0.02%	70.41%	0.951	1.14%	76.73%
2	1.289	0.71%	71.24%	0.619	7.07%	80.91%
3	0.929	69.87%	71.24%	0.506	85.77%	81.24%
4	0.518	69.87%	80.30%	0.328	86.31%	83.98%
5	0.41	69.90%	80.48%	0.265	86.70%	89.58%
6	0.31	78.96%	80.48%	0.205	90.56%	91.15%

Key nonlinear modeling assumptions are summarized as follows. The building was modeled in ETABS v23.1.1 using a three-dimensional frame model with rigid floor diaphragms. Nonlinear behavior of RC members was represented using a lumped-plasticity approach. As-built RC sections (including reinforcement) were defined using ETABS Section Designer (SD sections). Cracked-section stiffness modifiers were assigned following code-recommended values. Plastic hinge properties were generated using the ETABS built-in auto-hinge option based on ASCE 41-17, without user modification of the default force–deformation backbone (A–B–C–D–E). Flexural hinges were assigned at both ends of beams (M2–M3 hinges), and PMM interaction hinges were assigned at the top and bottom of columns at each story. No explicit shear hinges were introduced and shear/joint failure modes were not modeled.

Second-order P–Delta effects were included using the ETABS P-Delta option. Beam–column joints were modeled as rigid; rigid end zones and explicit panel-zone/joint shear deformation were not considered. Nonlinear static pushover analyses were performed independently in the X and Y directions. A first-mode (modal) lateral load pattern was adopted, and the roof diaphragm center of mass was used as the control point. The pushover capacity curve (base shear versus roof displacement) was converted to the ADRS format and combined with the demand spectrum using the CSM procedure described in Section 2.4 to determine the performance point. Engineering demand parameters (story drifts, member force demands, and hinge states) reported herein were extracted directly from the MDOF pushover step corresponding to the performance-point displacement.

For the retrofit configuration, the additional viscous damping provided by the VE dampers is quantified in terms of an effective first-mode damping ratio using the formulation in Equation (22). In the ETABS model, each story is assigned a lumped mass m_i, a tributary weight W_i, and a total equivalent viscous damping coefficient C_j representing all VE dampers installed at that level. The first-mode lateral participation factor ϕ_i and the relative deformation ϕ_{rj} across each damper are obtained from the modal analysis of the retrofitted structure. Table 2 summarizes the story-wise masses, damper distributions, combined damping coefficients, and the corresponding first-mode participation values used in the computation. The equivalent viscous coefficients C_j associated with nominal damper capacities of 500 kN, 750 kN, and 1000 kN are evaluated at the design shear strain and excitation frequency using the empirical calibration of the styrene–olefin-based VE material described in Section 2.1; representative fitting errors for this calibration are reported in Section 3.2 rather than the full proprietary regression formula. Substituting these coefficients, together with the fundamental period T of the retrofitted structure and the first-mode shape, into Equation (22) yields the overall effective damping ratio contributed by the VE dampers, which is then used in the capacity spectrum analysis and performance evaluation described in Section 3.

Table 2. Structural design parameters.

Story	W_i (kN)	m_i (t)	Total Number of Dampers	C_j	ϕ_i
RF	1176.79	119.99	0	0	1.000
6	1104.03	112.54	0	0	0.922
5	1104.03	112.54	16	63,000	0.804
4	1104.03	112.54	16	63,000	0.645
3	1104.03	112.54	16	63,000	0.456
2	1119.08	114.08	16	84,000	0.252

The effective seismic masses and the total damping coefficients of the VE dampers assigned to different stories in the ETABS model shown in Figure 11 are summarized in Table 2. For each story, the model specifies the tributary weight W_i, the lumped mass m_i, the total number of dampers, the combined damping coefficient C_j of the dampers at that story, and the first-mode participation value ϕ_i. The effective damping ratio ξ_{VE} contributed by all VE dampers is determined using the first modal period T of the structure, the story-wise damping coefficients, and the first-mode shape, as expressed by Equation (22).

For reproducibility of the building-level analyses, the VE dampers were implemented in ETABS using an equivalent Kelvin–Voigt form (a linear spring in parallel with a linear dashpot). The equivalent parameters were evaluated at a design shear strain amplitude γ = 300% (corresponding to a shear displacement amplitude of 30 mm for the 10 mm

VE layer thickness) and a representative ambient temperature T = 25 °C. The representative frequency was taken as $f = 1/T_{eq}$ corresponding to the equivalent period of the retrofitted structure at the performance point. Under these conditions, the equivalent spring stiffnesses adopted for the three damper ratings were K_{eq} = 24,000, 36,500, and 52,000 kN/m, respectively, while the corresponding dashpot coefficients were C_{eq} = 3500, 5250, 7000 kN·s/m, respectively. Identical parameters were assigned to all dampers of the same rating. This simplification is commonly adopted in design practice and was used here to avoid introducing unnecessary parameter variability without experimental support.

Notably, the maximum damper deformation obtained from the structural analysis was 15.1 mm ($\gamma \approx 151\%$), which is significantly smaller than the 30 mm amplitude associated with γ = 300%. Since the calibrated relationships indicate higher equivalent stiffness and damping at lower strain amplitudes, using parameters evaluated at γ = 300% provides a conservative basis for the building-level response assessment. Based on the calibrated relations, reducing the deformation amplitude from 30 mm to 15.1 mm would increase K_{eq} by approximately 54.6% and C_{eq} by approximately 57.2% for all damper ratings (the VE layer thickness is identical), implying that the reported seismic performance is not overestimated.

3. Results

This section presents the experimental results for the viscoelastic (VE) material under large shear strain and the seismic performance of the case-study hospital building before and after retrofit.

3.1. VE Material Behavior Under Large Shear Strain

As described in Section 2.1, cyclic tests were conducted on Styrene–olefin-based VE specimens at shear strain amplitudes of 300% and 400%, including both continuous loading and loading with a 24 h interval (INT.) introduced every 20 cycles. The evolution of the normalized equivalent shear modulus G_{eff} and the normalized equivalent damping ratio β_{eff} with the number of cycles is summarized in Figures 12–15. Solid line represents continuous loading specimen; dashed line represents intermittent loading specimen.

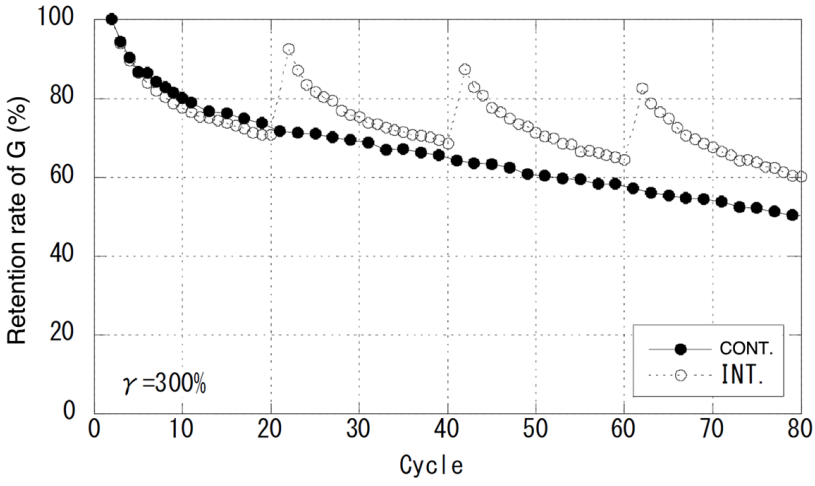


Figure 12. The rate of change in equivalent shear modulus G_{eff} under continuous and interval loading under shear strain 300%.

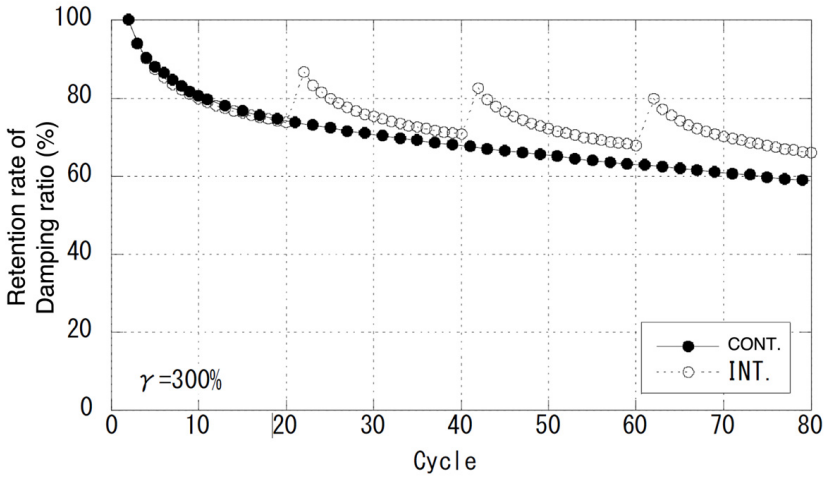


Figure 13. The rate of change in equivalent damping ratio β_{eff} under continuous and interval loading under shear strain 300%.

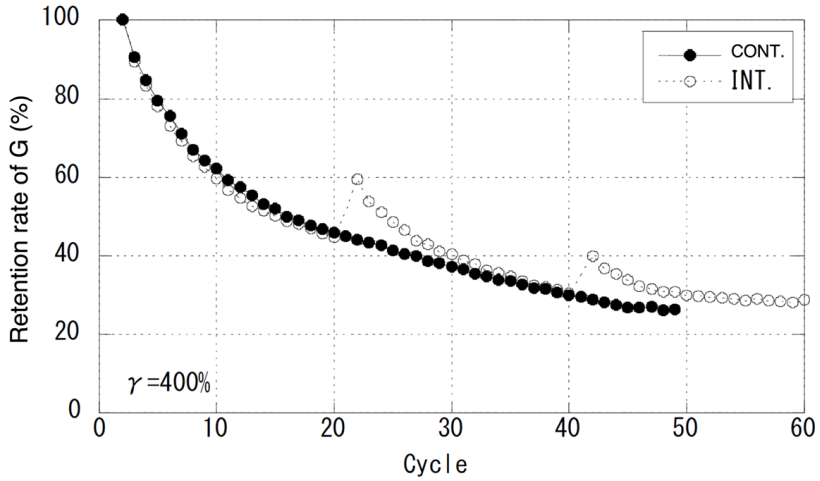


Figure 14. The rate of change in equivalent shear modulus G_{eff} under continuous and interval loading under shear strain 400%.

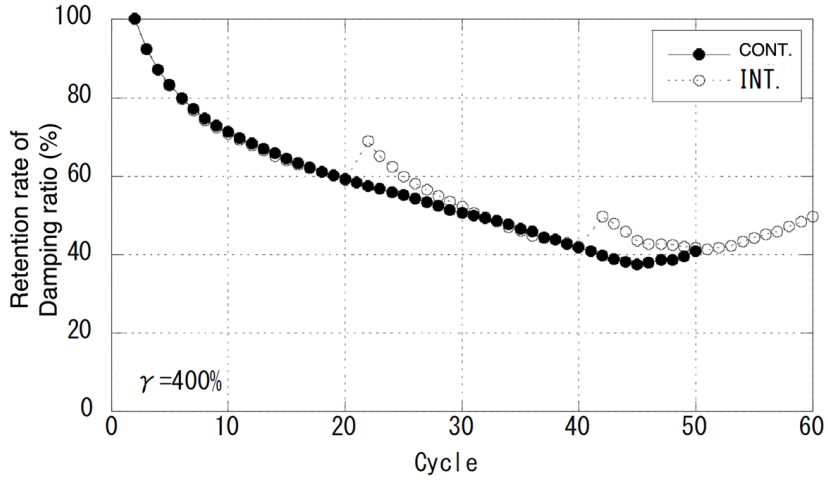


Figure 15. The rate of change in equivalent damping ratio β_{eff} under continuous and interval loading under shear strain 400%.

For a shear strain amplitude of 300%, Figures 12 and 13 show that under continuous loading the equivalent shear modulus G_{eff} decreases rapidly during the early cycles (e.g.,

by about 10% by cycle 3 and about 20% by cycle 10) and then degrades at a substantially reduced rate, approaching a long-duration plateau of approximately 60–65% after roughly 80 cycles. A similar monotonic reduction is observed for the equivalent damping ratio β_{eff}, which decreases toward approximately 60–65% over the same range of cycles. Under interval loading, both G_{eff} and β_{eff} exhibit a characteristic recovery at the beginning of each loading block following the 24 h rest period: the values at the start of each block are slightly higher than those immediately before unloading, but subsequently decay again toward levels comparable to the continuous loading case. Overall, at 300% shear strain, the long-term degradation trends under continuous and interval loading are close.

To avoid an arbitrary cycle selection for design, a degradation-rate–based post-transient criterion is adopted. Specifically, for a given effective property X (i.e., G_{eff} or β_{eff}), the reduction within a 5-cycle window is defined as $\Delta X(N) = (X_N - X_{N+5})/X_N$. The response is considered to have entered the post-transient regime when $\Delta X(N) \leq 5\%$. For γ = 300%, $\Delta G(9) \approx 5.2\%$ (cycles 9–14), whereas $\Delta G(10) \approx 4.9\%$ (cycles 10–15); meanwhile, β_{eff} satisfies the same criterion earlier (e.g., $\Delta\beta(7) < 5\%$ over cycles 7–12). Therefore, taking the more conservative onset cycle, $N_{\text{stab}} = \max(N_G, N_\beta) = 10$, the cycle-10 values are adopted as conservative design-effective parameters for engineering applications at γ = 300%. This choice is also consistent with the observed deceleration of degradation after the early cycles: while G_{eff} (and β_{eff}) has decreased by about 20% by cycle 10, the additional reduction from cycle 10 to cycle 30 is only on the order of 10 percentage points.

At a larger shear strain amplitude of 400%, Figures 14 and 15 indicate more severe degradation. Under continuous loading, the equivalent shear modulus drops steeply from 100% to about 40% within roughly 20 cycles and further decreases to approximately 25–30% by around 50 cycles. The equivalent damping ratio also decreases from 100% to below 40% over the same range of cycles. Under interval loading, the initial values at the start of each loading block again recover to levels higher than those immediately before unloading, and the retention ratios of both G_{eff} and β_{eff} remain slightly above those of the continuous loading case in the later cycles. Nevertheless, the overall reduction in stiffness and damping at 400% shear strain is significant, and the long-duration response after several tens of cycles is on the order of 30–40% of the initial properties.

Based on the above criterion, the design-effective values of G_{eff} and β_{eff} adopted in the design sheet and subsequent structural analyses were taken as the cycle-10 properties at the design shear strain amplitude γ = 300%, considering the consistency between the continuous- and interval-loading responses. These design-effective values were then used to define the VE damper parameters implemented in the case-study building and to evaluate the empirical expressions in Equations (4)–(7) at the design state.

Each curve in Figures 12–15 corresponds to a single tested specimen (n = 1 for each amplitude–protocol combination). For the first 20 cycles, the continuous and intermittent specimens at the same amplitude were subjected to an identical continuous loading history; over this common segment, the maximum relative difference in G_{eff} and C_{eff} between the two specimens was 2.7%, and the corresponding curves are visually nearly coincident.

3.2. Existing Condition and Seismic Performance of the Original Building

Modal properties of the as-built and retrofitted RC hospital models were obtained from elastic modal analyses. Table 1 summarizes the periods and effective modal mass participation ratios in the two principal horizontal directions. The building exhibits clear dominance of the first translational mode in each direction: Mode 1 (T = 1.67 s) contributes 70.4% of the effective mass in the Y direction, while Mode 3 (T = 0.929 s) contributes 69.2% of the effective mass in the X direction. The cumulative effective mass ratio of the first 12 modes reaches 93.8% in Y and 82.3% in X. Accordingly, nonlinear static (pushover)

analyses were conducted separately in each direction using a modal lateral load pattern based on the dominant translational mode shape (Mode 1 for Y and Mode 3 for X) and the standard equivalent SDOF transformation. This practice is consistent with commonly adopted nonlinear static procedures for regular mid-rise buildings with pronounced first-mode dominance, as described in FEMA 356/FEMA 440 and ASCE/SEI 41; dynamic procedures are recommended when higher-mode effects are expected to be significant. For retrofitted building, the first translational mode dominates the response in each principal direction, supporting the use of a modal (first-mode) load pattern for pushover and the equivalent SDOF transformation adopted herein.

In situ material tests were performed on the case-study hospital building to evaluate the condition of the existing RC members. Figure 9 summarizes the measured concrete compressive strengths and carbonation depths at each floor. The measured compressive strengths on all tested floors are significantly lower than the nominal design value of 210 kgf/cm^2, while the carbonation depths on most floors exceed the allowable limit of 4 cm. These results indicate deterioration in both load-carrying capacity and durability of the RC members after long-term service and environmental exposure.

According to the seismic evaluation guidelines adopted in this study [35–37], when the concrete strength falls below the design value and carbonation depths exceed the specified limit across a substantial portion of the structure, the building is classified as requiring seismic rehabilitation. On the basis of the test results shown in Figure 9 and the corresponding evaluation criteria, the hospital building falls into the category of structures that must be retrofitted.

For a residual service life of 20 years, the remaining-life-based design spectrum was derived from the original 475-year design spectrum following the procedure in Section 2.4.1, resulting in a reduced effective peak acceleration of a_{gr} = 0.228 g and an adjusted short-period spectral acceleration parameter S_{DS} = 0.57 (Figure 8). A nonlinear static pushover analysis of the original structure without VE dampers was performed, and the resulting capacity curve was converted into a capacity spectrum on the acceleration–displacement response spectrum (ADRS) plane using the first-mode participation factors defined in Equations (19) and (20). The reduced response spectrum for the remaining service life was then superimposed onto this capacity spectrum.

The intersection between the capacity spectrum and the reduced demand spectrum defines the performance point $(S_{d,p}^{\text{orig}}, S_{a,p}^{\text{orig}})$ and the corresponding ground acceleration index A_p^{orig} for the original structure. Under the adopted evaluation procedure, the demand spectrum for the bare structure is constructed for a nominal viscous damping ratio of 5%, which represents the baseline elastic damping of the RC frame [38]. Because no supplemental damping devices are present, the equivalent damping ratio at the performance point consists only of this baseline value and limited hysteretic contributions from the RC members and therefore remains close to 5%. The ADRS representation indicates that A_p^{orig} is lower than the reduced EPA value a_{gr} = 0.228 g, and the corresponding performance-point displacement is relatively large. Consequently, the original hospital building does not satisfy the target performance level in Stage III of the evaluation and requires seismic retrofit. At the performance-point displacement, the peak interstory drift ratio reaches 1.67% in the Y direction (0.52% in the X direction), exceeding the adopted 1.5% drift objective and further confirming the need for seismic rehabilitation.

3.3. Seismic Performance of the Retrofitted Building

To meet the seismic performance requirements while maintaining hospital operations, a retrofit scheme incorporating VE dampers was implemented. The construction routes and installation locations of the VE dampers, with nominal maximum force capacities of

500 kN, 750 kN, and 1000 kN on the second through fifth stories, are shown in Figure 10, and the corresponding ETABS model of the retrofitted building is shown in Figure 11. The story-wise tributary weights, lumped masses, total number of dampers, combined damping coefficients C_j, and first-mode participation values ϕ_i used in the numerical model are summarized in Table 2.

Using the damping coefficients corresponding to damper capacities of 500 kN, 750 kN, and 1000 kN (taken as 3500 kN·s/m, 5250 kN·s/m, and 7000 kN·s/m, respectively, calculated by Equation (12)) and a fundamental period of the damped structure of T = 0.951 s with damper installation angle $\theta_j = 0^\circ$, the effective first-mode damping ratio contributed by all VE dampers, ξ_{VE}, was evaluated by Equation (22). The resulting VE contribution is ξ_{VE} = 7.92%.

Nonlinear pushover analysis of the retrofitted structure yields a spectral acceleration and spectral displacement at the performance point of

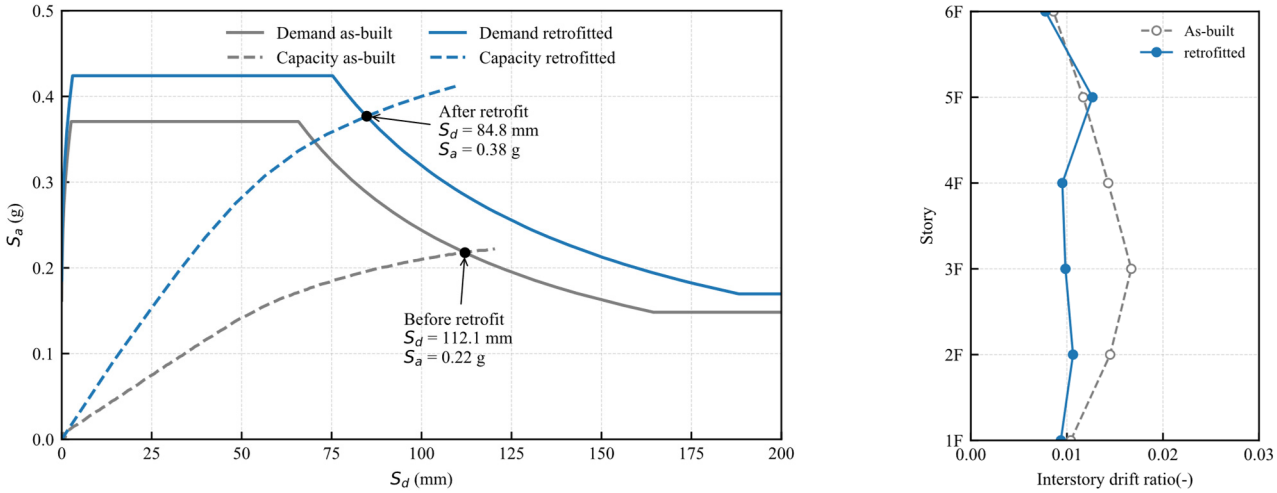
$$S_{a,p}^{\mathrm{retro}} = 0.3768\ g, \quad S_{d,p}^{\mathrm{retro}} = 8.4691\ \mathrm{cm}$$

The corresponding equivalent period, raw hysteretic damping ratio, and total equivalent damping ratio at the performance point are T_{eq} = 0.9510 s, ξ_{h} = 0.1897 (18.97%), and ξ_{eq} = 0.1918 (19.18%), respectively. Accordingly, the effective hysteretic contribution in Equation (23) is $\kappa\xi_{\mathrm{h}}$ = 0.0626 (6.26%) with κ = 0.33.

Using the damping modification factors associated with ξ_{eq} provided in the current building code [38], the transition period of the damping-modified demand spectrum is computed as T_0 = 1.3864 s with B_S = 1.5779 and B_1 = 1.4795. Substituting these values into Equation (24) gives the ground acceleration index associated with the performance point, $A_p^{\mathrm{retro}} = 0.2379g$. This value exceeds the reduced effective peak acceleration a_{gr} = 0.228 g by 0.0099 g (A_p/a_{gr} = 1.043), indicating that the retrofit meets the target performance level but with a relatively small reserve.

To quantify the robustness of this near-threshold margin, a deterministic sensitivity check was performed by perturbing the equivalent damping components that govern $B_S(\xi_{eq})$. Specifically, ξ_{VE} and the hysteretic contribution $\kappa\xi_{\mathrm{h}}$ were reduced by 10% and 20% to reflect (a) modeling and parameter-estimation uncertainty and (b) potential short-term degradation effects. Re-evaluating $B_S(\xi_{eq})$ and A_p using Equation (24) shows that A_p decreases from 0.2379 g (baseline) to 0.231 g when ξ_{VE} is reduced by 20% alone, and to 0.226 g when both ξ_{VE} and $\kappa\xi_{\mathrm{h}}$ are reduced by 20% simultaneously. These results confirm that the retrofit is calibrated close to the minimum level required to satisfy the target performance, and they highlight the importance of conservative damping inputs and modeling fidelity when the performance check is near the threshold.

The ADRS representation of both the original and retrofitted configurations, including the capacity spectra, the (damping-modified) demand spectra, and the corresponding performance points, is shown in Figure 16a. Compared with the original configuration, the retrofit increases the ground acceleration index at the performance point from A_p^{orig} to $A_p^{\mathrm{retro}} = 0.2379g$ and reduces the spectral displacement from $S_{d,p}^{\mathrm{orig}}$ to $S_{d,p}^{\mathrm{retro}}$ = 8.4691 cm. In terms of global energy dissipation, the effective viscous damping ratio increases from about 5% for the bare structure—representing only baseline elastic and limited hysteretic damping—to approximately 19% for the retrofitted building when the VE dampers and structural hysteresis are both taken into account. This substantial increase in equivalent damping, together with the moderate increase in effective stiffness, explains the reduction in displacement demand and the improved seismic capacity observed in the capacity spectrum analysis.



(**a**) (**b**)

Figure 16. Seismic performance evaluation before and after retrofit: (**a**) ADRS representation with capacity/demand spectra and performance points; (**b**) Y-direction interstory drift ratio profiles at the CSM performance point.

Figure 16b compares the Y-direction interstory drift ratio profiles at the CSM performance point. The maximum Y-direction drift ratio decreases from 1.67% in the as-built configuration to 1.27% after retrofit, with the peak demand occurring at the 3rd story in both cases. A clear reduction is observed at the retrofit stories where VE dampers are installed (2F–5F), indicating that the supplemental damping effectively suppresses drift demands in the targeted range. In contrast, the drift ratios at stories without dampers (1F and 6F) remain at similar levels before and after retrofit, suggesting that the retrofit primarily redistributes and reduces deformation demands within the instrumented stories rather than uniformly altering the response over the full height. By comparison, the X-direction peak drift ratio is below the 1.5% objective in both configurations (0.52% as-built and 0.39% retrofitted) and is therefore not governing.

3.4. Practical Aspects of Construction

Construction and completion photographs of the retrofitted hospital building are shown in Figure 17.

The images indicate that the VE dampers and their supporting steel brackets were installed using dry construction methods. Prefabricated damper assemblies and steel connection components were brought to the site and attached to the existing RC frame through bolted and anchored steel plates, avoiding on-site concrete casting in the patient areas. Interior photographs (Figure 17a) illustrate the installation of damper units and steel components within ceiling spaces and service corridors, while exterior views (Figure 17b) show that the retrofit was executed with minimal alteration to the building façade and streetscape.

Because the hospital had to remain operational throughout the retrofit, construction activities were organized to limit interference with daily medical services. Work was staged by floor and by bay, with temporary partitions and local access control used to isolate the construction zones from occupied areas. The use of prefabricated VE dampers and steel components reduced on-site wet trades, shortened the construction duration, and minimized dust and noise, allowing the retrofit to be carried out without prolonged shutdown of clinical functions. These practical observations confirm that VE-damper-based seismic retrofit schemes are compatible with the operational constraints of critical facilities

such as hospitals, complementing the analytical performance improvements demonstrated by the capacity spectrum results.



(**a**)



(**b**)

Figure 17. Construction and completion photos of the hospital building equipped with VE dampers. (**a**) Construction photos. (**b**) Completion photos.

4. Discussion

4.1. Large-Strain Behavior and Empirical Modeling of VE Dampers

The large-strain cyclic tests at 300% and 400% shear strain provide direct evidence of how the viscoelastic properties evolve under demands comparable to, or exceeding, those expected in severe earthquakes. At 300% shear strain, both the equivalent shear modulus G_{eff} and the equivalent damping ratio βeff exhibit rapid degradation during the first few cycles, followed by gradual stabilization: under continuous loading, G_{eff} decreases during the early cycles and then degrades at a substantially reduced rate after 10 cycles, approaching 60–65% after roughly 80 cycles; β_{eff} exhibits a similar trend (Figures 12 and 13). Under interval loading with 24 h rest every 20 cycles, a modest "recovery" is observed at the start of each loading block, but the long-term degradation trends of G_{eff} and β_{eff} remain close to those under continuous loading at this deformation level.

At 400% shear strain, the degradation becomes significantly more pronounced (Figures 14 and 15). Under continuous loading, G_{eff} falls from 100% to about 40% within roughly 20 cycles and further decreases to about 25–30% by 50 cycles; β_{eff} likewise decreases from 100% to below 40% over the same range of cycles. Under interval loading, recovery is again observed at the beginning of each loading segment, and the retention ratios of both G_{eff} and β_{eff} remain slightly higher than those under continuous loading in the later cycles, indicating that rest periods can partially mitigate stiffness and damping degradation at very large strains, although the net reduction remains substantial.

These results clarify that (a) at deformation levels around 300%, rest intervals have limited influence on long-term degradation, whereas (b) at 400% and above, the material is more sensitive to cumulative damage and benefits more from intermittent unloading.

Together with the small-specimen tests up to 450% shear strain reported in the companion study, which show that the styrene-olefin-based material remains intact without fracture even under such extreme deformation, the present data confirm that the adopted VE material can sustain repeated large shear deformations while still providing substantial energy dissipation. For seismic design, this implies that (a) design values of G_{eff} and β_{eff} should be selected near the long-duration plateau (rather than the initial cycles), and (b) for beyond-design-level demands corresponding to shear strains approaching 400%, lower-bound properties consistent with the more severe degradation should be adopted. The experimental trends also justify the use of empirical correction/adjustment formulas in the engineering design sheet to map test results at different amplitudes and temperatures to the chosen design state.

Based on the combined dataset of small-specimen and large-strain tests, the mechanical properties of the VE dampers were expressed through empirical relationships linking effective stiffness, damping coefficient, and damping ratio to shear strain and temperature. These relationships are implemented in the design sheet in closed-form functional expressions, while the numerical regression coefficients are kept proprietary. Even though the individual coefficients are not disclosed, the regression reproduces the measured properties with global relative errors on the order of 10%, which is adequate for preliminary and practical design applications. The disclosure of the functional form, together with reported error measures and representative experimental curves, ensures that the modeling approach is transparent and allows independent verification of its reasonableness without revealing manufacturer-sensitive details.

4.2. Seismic Performance Evaluation and Role of VE Dampers

The seismic evaluation framework combines a remaining-life-based design spectrum with a capacity spectrum method in order to maintain consistency with modern performance-based design principles. The reduced elastic demand spectrum is first derived by scaling the code-based 5%-damped spectrum to the target remaining life of the existing building, and the nonlinear capacity curve of the structure is converted into an equivalent SDOF capacity spectrum. The total equivalent damping ratio at the performance point is then determined by combining: (i) the inherent (5%) viscous damping, (ii) the hysteretic damping of the RC structure, computed from the area of the SDOF hysteresis loop at the performance-point displacement, and (iii) the additional effective damping ratio contributed by all VE dampers, evaluated on the basis of the Kelvin–Voigt model and first-mode participation (Equations (21)–(23)).

This procedure yields a self-consistent equivalent damping ratio ξ_{eq} and corresponding demand spectrum, enabling direct comparison between the performance point and the reduced hazard level associated with the desired remaining life.

For the retrofitted hospital building, the modal damping ratio provided by the VE dampers is computed using Equation (22). With story-wise damper damping coefficients C_j of 3500, 5250, and 7000 kN·s/m for nominal capacities of 500, 750, and 1000 kN, respectively, and a fundamental period of T = 0.951 s, the effective damping ratio contributed by the VE dampers is 7.92%.

Nonlinear pushover analysis of the retrofitted structure yields a performance point with spectral acceleration $S_{a,p}$ = 0.3768 g and spectral displacement $S_{d,p}$ = 8.4691 cm. The corresponding equivalent period T_{eq}, hysteretic damping ratio ξ_{h}, and total equivalent damping ratio ξ_{eq}, obtained from Equations (21)–(23) and the SDOF hysteresis loop area,

are T_{eq} = 0.9510 s, ξ_h = 0.1897 (18.97%), and ξ_{eq} = 0.1918 (19.18%), respectively; thus, $\kappa\xi_h$ = 0.0626 (6.26%) in Equation (23) (κ = 0.33).

Using damping modification factors from the current building code, the transition period T_0 and the damper-modified demand spectrum are constructed, and the ground acceleration associated with the performance point is evaluated as A_p = 0.2379 g. This value slightly exceeds the reduced effective peak acceleration a_{gr} = 0.228 g derived from the remaining-life-based demand spectrum, indicating that the retrofit scheme satisfies the target performance with a modest safety margin.

Two observations follow from these results. First, while the VE dampers themselves provide an effective damping ratio of about 8%, the total equivalent damping ratio at the performance point, including structural hysteresis, reaches nearly 19%, which corresponds to a significant reduction in demand relative to the original 5%-damped spectrum. Second, the fact that A_p slightly exceeds a_{gr}, rather than greatly exceeding it, suggests that the retrofit scheme is calibrated close to the minimum level required to meet the target performance, which is desirable from an economic perspective but also highlights the importance of accurate damping estimation and capacity modeling.

4.3. Practical Implications for Hospital Retrofits

From a practical standpoint, the case-study hospital illustrates both the advantages and the engineering constraints associated with VE-damper retrofits in operational healthcare facilities. Construction and completion photographs (Figure 17) show that the dampers and their supporting steel frames were installed using dry construction methods—primarily bolted steel components anchored to existing RC beams and columns—without major wet works or extensive demolition.

This allowed most medical services to remain in operation during construction, with only localized and short-term disruptions in the vicinity of the work areas. The ability to retrofit from the exterior or from circulation zones, while leaving structural walls and most interior finishes undisturbed, is a notable advantage of VE dampers over more intrusive strengthening methods such as jacketing or additional RC walls.

On the other hand, the introduction of VE dampers inevitably modifies the internal force paths in the existing structure. The axial forces and shear forces transmitted through the steel braces and dampers generate additional bending moments and shears in the supporting beams and columns. As noted in the design and analysis of the case-study building, these effects may require local strengthening of RC beams (e.g., by adding steel plates or externally bonded reinforcement) and careful detailing of anchorage zones to avoid premature failure or excessive cracking under damper-induced actions.

In practice, therefore, the attractiveness of VE dampers for hospital retrofits stems not only from their energy-dissipation ability and constructability, but also from the feasibility of integrating them with existing load paths without introducing new weak links.

4.4. Limitations and Future Research

Several limitations of the present study should be recognized. First, the large-strain cyclic tests of the VE material were conducted under harmonic loading at a single low frequency (approximately 0.33 Hz) and at two deformation levels (300% and 400% shear strain) with a fixed rest-interval pattern.

Although these conditions are representative of large, low-frequency demands, they do not cover the full range of frequency content, amplitude histories, and multi-directional effects that may occur in real earthquakes. Additional testing over a broader range of frequencies, variable-amplitude loading histories, and environmental conditions (e.g., long-term aging, temperature cycles) is needed to fully characterize the durability and

rate dependence of the material. A broader frequency sweep was not pursued in the present large-strain degradation campaign in order to limit confounding thermal and cumulative-damage effects; this will be addressed in future work.

Second, the building-level seismic evaluation relies on an equivalent SDOF representation and nonlinear pushover analysis, with total damping estimated from equivalent hysteretic and viscous contributions in the first mode.

This approach is consistent with current guidelines and practical for engineering design, but it neglects higher-mode effects and record-to-record variability that would be captured in multi-degree-of-freedom nonlinear time-history analyses. The adequacy of the retrofit solution for irregular structures or for sites with complex seismic hazard characteristics should therefore be confirmed by more detailed dynamic analyses when warranted.

Third, the empirical regression model used in the design sheet is calibrated from a finite set of test data, and the numerical coefficients are not disclosed. While the functional form is presented and the regression accuracy is quantified at the global level, extrapolation beyond the tested ranges of temperature and shear strain should be undertaken with caution, preferably supported by additional laboratory data. Finally, the conclusions drawn from the hospital case study are based on a single building with specific geometry, detailing, and site conditions; more case studies and, ideally, post-earthquake performance observations would be valuable for validating and refining the proposed methodology.

Future work should therefore focus on: (a) expanding the experimental database for styrene-olefin-based VE materials under multi-frequency, multi-axial, and long-duration loading; (b) conducting nonlinear time-history analyses with suites of ground motions to quantify the dispersion in performance measures for VE-damper retrofitted buildings; and (c) implementing monitoring programs on retrofitted hospitals and other critical facilities to observe the in-service behavior and long-term stability of VE dampers. These efforts would help to generalize the present findings and further strengthen the engineering basis for adopting VE dampers in seismic retrofitting practice.

5. Conclusions

Based on the experimental investigations and analytical studies presented in this work, the following conclusions can be drawn:

(1) The styrene-olefin-based viscoelastic material used in the dampers exhibits stable, though degrading, mechanical behavior under large shear strains up to 300–400%. At 300% shear strain, both equivalent shear modulus and equivalent damping ratio degrade rapidly in the first few cycles and then approach a plateau at about 60–65% of their initial values; at 400% shear strain, the degradation is more pronounced, with G_{eff} and β_{eff} decreasing to roughly 25–30% and below 40%, respectively, by 50 cycles. Interval loading with 24 h rest periods introduces partial recovery but does not fundamentally change the long-term trends. Together with small-specimen tests up to 450% shear strain, which show that the material remains intact without fracture, these results confirm that the adopted VE material is suitable for repeated large-deformation energy dissipation.

(2) An empirical modeling framework has been established in which the effective stiffness, damping coefficient, and damping ratio of the VE dampers are expressed as functions of shear strain and ambient temperature, calibrated from an extensive set of laboratory data. The functional forms of these relationships are provided in the paper, while the regression coefficients—derived using least-squares fitting—are treated as proprietary. Even without disclosing the coefficients, the model reproduces the measured properties with typical relative errors on the order of 10%, providing a practical and reasonably accurate tool for design offices to evaluate VE damper properties at arbitrary target conditions within the calibrated range.

(3) A seismic evaluation framework combining a remaining-life-based demand spectrum with a capacity spectrum approach has been applied to a six-story RC hospital building. For the retrofitted structure, nonlinear pushover analysis and equivalent-damping calculations yield a performance-point spectral acceleration $S_{a,p}$ = 0.3768 g, spectral displacement $S_{d,p}$ = 8.4691 cm, equivalent period T_{eq} = 0.9510 s, hysteretic damping ratio ξ_{h} = 0.1897 with $\kappa\xi_{\mathrm{h}}$ = 0.0626 (6.26%), and total equivalent damping ratio ξ_{eq} = 0.1918. The corresponding ground acceleration at the performance point, A_p = 0.2379 g, slightly exceeds the reduced effective peak acceleration a_{gr} = 0.228 g obtained from the remaining-life-based spectrum, indicating that the retrofit meets the target performance level.

(4) The VE dampers provide an effective damping ratio of about 7.92% at the performance point, and, in combination with structural hysteresis, increase the total equivalent damping ratio of the building to nearly 19%. This substantial enhancement in damping, achieved without major changes to the primary RC lateral-force-resisting system, is a key factor in satisfying the performance-based seismic criteria for the existing hospital. The case study also demonstrates that VE dampers can be installed using dry construction methods with minimal disruption to hospital operations, making them particularly attractive for critical facilities that must remain functional during retrofit works.

(5) Although the methodology and case study presented here illustrate the feasibility and effectiveness of VE-damper retrofits for existing RC buildings, the results are subject to limitations related to the scope of the experimental data, the single-building nature of the application, and the use of equivalent SDOF pushover analysis. Further experimental research, numerical simulations, and field observations are needed to extend the proposed empirical models to broader ranges of loading and environmental conditions, to assess the robustness of the remaining-life-based evaluation framework for different structural configurations, and to accumulate additional evidence on the long-term performance of VE dampers in real structures.

Author Contributions: Conceptualization, S.L.; methodology, S.L.; software, S.L.; formal analysis, S.L.; investigation, S.L. and C.J.; resources, S.L.; writing—original draft preparation, S.L.; writing—review and editing, C.J.; visualization, C.J.; All authors have read and agreed to the published version of the manuscript.

Funding: This research was funded by The State Key Laboratory Basic Research Funding Program of the Ministry of Science and Technology of China, grant number SLDRCE19-A-10.

Data Availability Statement: The viscoelastic material test data and the detailed regression coefficients of the proprietary material model are not publicly available due to confidentiality agreements with the damper manufacturer. Aggregated statistics, design values of the viscoelastic properties, and all structural analysis results are provided within the article.

Conflicts of Interest: The authors declare no conflicts of interest.

References

1. FEMA 356. *Prestandard and Commentary for the Seismic Rehabilitation of Buildings*; Federal Emergency Management Agency: Washington, DC, USA, 2000.
2. Antoniou, S. *Seismic Retrofit of Existing Reinforced Concrete Buildings*; John Wiley & Sons: Hoboken, NJ, USA, 2023.
3. Zameeruddin, M.; Sangle, K.K. Review on Recent developments in the performance-based seismic design of reinforced concrete structures. *Structures* **2016**, *6*, 119–133. [CrossRef]
4. Basereh, S.; Okumus, P.; Aaleti, S. Seismic retrofit of reinforced concrete shear walls to ensure reparability. In *Structures Congress*; American Society of Civil Engineers: Reston, VA, USA, 2020; pp. 498–509.
5. Chang, S.Y.; Chen, T.W.; Tran, N.C.; Liao, W.I. Seismic retrofitting of RC columns with RC jackets and wing walls with different structural details. *Earthq. Eng. Eng. Vib.* **2014**, *13*, 279–292. [CrossRef]
6. Thermou, G.E.; Elnashai, A.S. Seismic retrofit schemes for RC structures and local-global consequences. *Prog. Struct. Eng. Mater.* **2006**, *8*, 1–15. [CrossRef]

7. Code, U.B. *Uniform Building Code*; International Conference of Building Officials: Whittier, CA, USA, 1997.
8. Ching, F.D.; Winkel, S.R. *Building Codes Illustrated: A Guide to Understanding the 2021 International Building Code*; John Wiley & Sons: Hoboken, NJ, USA, 2021.
9. Badoux, M.; Jirsa, J.O. Steel bracing of RC frames for seismic retrofitting. *J. Struct. Eng.* **1990**, *116*, 55–74. [CrossRef]
10. Cao, X.Y.; Shen, D.; Feng, D.C.; Wang, C.L.; Qu, Z.; Wu, G. Seismic retrofitting of existing frame buildings through externally attached sub-structures: State of the art review and future perspectives. *J. Build. Eng.* **2022**, *57*, 104904. [CrossRef]
11. Tsai, K.C.; Hsu, C.H.; Li, C.H.; Chin, P.Y. Experimental and analytical investigations of steel panel dampers for seismic applications in steel moment frames. *Earthq. Eng. Struct. Dyn.* **2018**, *47*, 1416–1439. [CrossRef]
12. Lu, Z.; Wang, Z.; Zhou, Y.; Lu, X. Nonlinear dissipative devices in structural vibration control: A review. *J. Sound Vib.* **2018**, *423*, 18–49. [CrossRef]
13. Ferraioli, M.; Lavino, A.; De Matteis, G. A design method for seismic retrofit of reinforced concrete frame buildings using aluminum shear panels. *Arch. Civ. Mech. Eng.* **2023**, *23*, 106. [CrossRef]
14. Kim, J.; An, S. Optimal distribution of friction dampers for seismic retrofit of a reinforced concrete moment frame. *Adv. Struct. Eng.* **2017**, *20*, 1523–1539. [CrossRef]
15. Eskandari Nasab, M.S.; Javidan, M.M.; Chun, S.; Kim, J. Experimental study on seismic retrofit of a RC frame using viscoelastic dampers. *Structures* **2021**, *34*, 771–786. [CrossRef]
16. Guo, T.; Xu, J.; Xu, W.; Di, Z. Seismic Upgrade of Existing Buildings with Fluid Viscous Dampers: Design Methodologies and Case Study. *J. Perform. Constr. Facil.* **2015**, *29*, 04014175. [CrossRef]
17. Shen, H.; Zhang, R.; Weng, D.; Ge, Q.; Wang, C.; Islam, M.M. Design method of structural retrofitting using viscous dampers based on elastic–plastic response reduction curve. *Eng. Struct.* **2020**, *208*, 109917. [CrossRef]
18. Hu, S.; Hao, H.; Meng, D.; Yang, M. Theoretical and numerical study of the thermo-mechanical coupling effect on the fluid viscous damper. *J. Sound Vib.* **2025**, *597*, 118846. [CrossRef]
19. Hu, R.; Hu, S.; Yang, M.; Meng, D. Experimental study on the coordinated behavior of the Combined Viscous-Steel Damping System (CVSDS) for multi-level seismic mitigation. *Structures* **2023**, *57*, 105344. [CrossRef]
20. Mahrenholtz, C.; Lin, C.-C.; Rolfes, R. Retrofit of reinforced concrete frames with buckling-restrained braces. *Earthq. Eng. Struct. Dyn.* **2015**, *44*, 59–78. [CrossRef]
21. Pan, K.-Y.; Wu, A.-C.; Tsai, K.-C.; Li, C.-H.; Khoo, H.-H. Seismic retrofit of reinforced concrete frames using buckling-restrained braces with bearing block load transfer mechanism. *Earthq. Eng. Struct. Dyn.* **2016**, *45*, 2303–2326. [CrossRef]
22. Alam, Z.; Zhang, C.; Samali, B. The role of viscoelastic damping on retrofitting seismic performance of asymmetric reinforced concrete structures. *Earthq. Eng. Eng. Vib.* **2020**, *19*, 223–237. [CrossRef]
23. Shen, K.L.; Soong, T.T. Modeling of viscoelastic dampers for structural applications. *J. Eng. Mech.* **1995**, *121*, 694–701. [CrossRef]
24. Aprile, A.; Inaudi, J.A.; Kelly, J.M. Evolutionary model of viscoelastic dampers for structural applications. *J. Eng. Mech.* **1997**, *123*, 551–560. [CrossRef]
25. Samali, B.; Kwok, K.C.S. Use of viscoelastic dampers in reducing wind- and earthquake-induced motion of building structures. *Eng. Struct.* **1995**, *17*, 639–654. [CrossRef]
26. Gu, H.S.; Itoh, Y. Ageing behaviour of natural rubber and high damping rubber materials used in bridge rubber bearings. *Adv. Struct. Eng.* **2010**, *13*, 1105–1113. [CrossRef]
27. Xu, Z.D.; Liao, Y.X.; Ge, T.; Xu, C. Experimental and theoretical study of viscoelastic dampers with different matrix rubbers. *J. Eng. Mech.* **2016**, *142*, 04016051. [CrossRef]
28. Zhou, Y.; Liu, X.F.; Wang, M. Experimental study on mechanical properties of two types of viscoelastic dampers. *Eng. Mech.* **2021**, *38*, 167–177. (In Chinese)
29. Ismail, M.; Ikhouane, F.; Rodellar, J. The hysteresis Bouc-Wen model, a survey. *Arch. Comput. Methods Eng.* **2009**, *16*, 161–188. [CrossRef]
30. Shanks, R.A.; Kong, I. General purpose elastomers: Structure, chemistry, physics and performance. In *Advances in Elastomers I. Advanced Structured Materials, 11*; Visakh, P., Thomas, S., Chandra, A., Mathew, A., Eds.; Springer: Berlin/Heidelberg, Germany, 2013.
31. Okui, N. Relationships between melting temperature, maximum crystallization temperature and glass transition temperature. *Polymer* **1990**, *31*, 92–94. [CrossRef]
32. Makris, N.; Constantinou, M.C. Models of Viscoelasticity with Complex-Order Derivatives. *J. Eng. Mech.* **1993**, *119*, 1453–1464. [CrossRef]
33. Soong, T.T.; Dargush, G.F. *Passive Energy Dissipation Systems in Structural Engineering*; John Wiley & Sons: Hoboken, NJ, USA, 1997.
34. Christopoulos, C.; Filiatrault, A. *Principles of Passive Supplemental Damping and Seismic Isolation*; IUSS Press: Vienna, Austria, 2006.
35. Chung, L.L.; Yeh, Y.K.; Chien, W.-Y.; Chai, J.F.; Hsiao, F.P.; Shen, W.C.; Chiu, C.C.; Chou, T.K.; Chao, Y.F.; Yang, Y.S.; et al. *Technology Handbook for Seismic Evaluation and Retrofit of School Buildings*; National Center for Research on Earthquake Engineering (NCREE-08-023): Taipei, Taiwan, 2008. (In Chinese)

36. Chung, L.L.; Yeh, Y.K.; Chien, W.Y.; Hsiao, F.P.; Shen, W.C.; Chiu, C.C.; Chou, T.K.; Chao, Y.F.; Yang, Y.S.; Tu, Y.H.; et al. *Technology Handbook for Seismic Evaluation and Retrofit of School Buildings*, 2nd ed.; National Center for Research on Earthquake Engineering (NCREE-09-023): Taipei, Taiwan, 2009. (In Chinese)
37. Hsiao, F.P.; Chung, L.L.; Yeh, Y.K.; Chien, W.Y.; Shen, W.C.; Chiu, C.C.; Chou, T.K.; Chao, Y.F.; Weng, P.W.; Yang, Y.S.; et al. *Technology Handbook for Seismic Evaluation and Retrofit of School Buildings*, 3rd ed.; National Center for Research on Earthquake Engineering (NCREE-13-023): Taipei, Taiwan, 2013. (In Chinese)
38. Building Administration Division. *Seismic Design Specifications and Commentary of Buildings, Construction and Planning Agency*; Ministry of the Interior: Taipei, Taiwan, 2024. (In Chinese)
39. Tien, C.C.; Lo, J.H.; Tsai, Y.C.; Chang, K.C.; Huang, Y.-H. *Seismic Safety Assessment and Retrofit Criteria for Telecommunication and Transportation Systems*; (CEER R85-01); Center for Earthquake Engineering Research: Taipei, Taiwan; National Taiwan University: Taipei, Taiwan, 1996.

Disclaimer/Publisher's Note: The statements, opinions and data contained in all publications are solely those of the individual author(s) and contributor(s) and not of MDPI and/or the editor(s). MDPI and/or the editor(s) disclaim responsibility for any injury to people or property resulting from any ideas, methods, instructions or products referred to in the content.